

University of Nebraska - Lincoln

DigitalCommons@University of Nebraska - Lincoln

---

ANDRILL Research and Publications

Antarctic Drilling Program

---

2010

**$^{40}\text{Ar}-^{39}\text{Ar}$  dating of volcanogenic products from the AND-2A core (ANDRILL Southern McMurdo Sound Project, Antarctica): Correlations with the Erebus Volcanic Province and implications for the age model of the core**

Gianfranco Di Vincenzo

*Istituto di Geoscienze e Georisorse, CNR, Pisa, Italy, g.divincenzo@igg.cnr.it*

Laura Bracciali

*Università di Pisa*

Paola Del Carlo

*Istituto Nazionale di Geofisica e Vulcanologia, Pisa, Italy*

Kurt Panter

*Bowling Green State University, kpanter@bgsu.edu*

Sergio Rocchi

*Università di Pisa*

Follow this and additional works at: <https://digitalcommons.unl.edu/andrillrespub>



Part of the [Environmental Indicators and Impact Assessment Commons](#)

---

Di Vincenzo, Gianfranco; Bracciali, Laura; Del Carlo, Paola; Panter, Kurt; and Rocchi, Sergio, " $^{40}\text{Ar}-^{39}\text{Ar}$  dating of volcanogenic products from the AND-2A core (ANDRILL Southern McMurdo Sound Project, Antarctica): Correlations with the Erebus Volcanic Province and implications for the age model of the core" (2010). *ANDRILL Research and Publications*. 52.

<https://digitalcommons.unl.edu/andrillrespub/52>

This Article is brought to you for free and open access by the Antarctic Drilling Program at DigitalCommons@University of Nebraska - Lincoln. It has been accepted for inclusion in ANDRILL Research and Publications by an authorized administrator of DigitalCommons@University of Nebraska - Lincoln.

# $^{40}\text{Ar}$ - $^{39}\text{Ar}$ dating of volcanogenic products from the AND-2A core (ANDRILL Southern McMurdo Sound Project, Antarctica): Correlations with the Erebus Volcanic Province and implications for the age model of the core

Gianfranco Di Vincenzo,<sup>1</sup> Laura Bracciali,<sup>2</sup> Paola Del Carlo,<sup>3</sup> Kurt Panter,<sup>4</sup> and Sergio Rocchi<sup>2</sup>

1. Istituto di Geoscienze e Georisorse, CNR, via Moruzzi 1, I-56124 Pisa, Italy

2. Dipartimento di Scienze della Terra, Università di Pisa, Via S. Maria 53, I-56126 Pisa, Italy

3. Sezione di Pisa, Istituto Nazionale di Geofisica e Vulcanologia, via della Faggiola 32, I-56126 Pisa, Italy

4. Department of Geology, Bowling Green State University, Bowling Green, OH 43403, USA

Corresponding author – Gianfranco Di Vincenzo, email [g.divincenzo@igg.cnr.it](mailto:g.divincenzo@igg.cnr.it)

## Abstract

The AND-2A drillcore (Antarctic Drilling Program—ANDRILL) was successfully completed in late 2007 on the Antarctic continental margin (Southern McMurdo Sound, Ross Sea) with the aim of tracking ice proximal to shallow marine environmental fluctuations and to document the 20-Ma evolution of the Erebus Volcanic Province. Lava clasts and tephra layers from the AND-2A drillcore were investigated from a petrographic and stratigraphic point of view and analyzed by the  $^{40}\text{Ar}$ - $^{39}\text{Ar}$  laser technique in order to constrain the age model of the core and to gain information on the style and nature of sediment deposition in the Victoria Land Basin since Early Miocene. Ten out of 17 samples yielded statistically robust  $^{40}\text{Ar}$ - $^{39}\text{Ar}$  ages, indicating that the AND-2A drillcore recovered  $\leq 230$  m of Middle Miocene ( $\sim 128$ – $358$  m below sea floor,  $\sim 11.5$ – $16.0$  Ma) and  $> 780$  m of Early Miocene ( $\sim 358$ – $1093$  m below sea floor,  $\sim 16.0$ – $20.1$  Ma). Results also highlight a nearly continuous stratigraphic record from at least 358 m below sea floor down hole, characterized by a mean sedimentation rate of  $\sim 19$  cm/ka, possible oscillations of no more than a few hundreds of ka and a break within  $\sim 17.5$ – $18.1$  Ma. Comparison with available data from volcanic deposits on land, sug-

gests that volcanic rocks within the AND-2A core were supplied from the south, possibly with source areas closer to the drill site for the upper core levels, and from 358 m below sea floor down hole, with the “proto-Mount Morning” as the main source.

**Keywords:** ANDRILL SMS,  $^{40}\text{Ar}$ - $^{39}\text{Ar}$  geochronology, Erebus volcanic province, McMurdo Sound, Lava clasts, Sedimentation rate, Tephra layers, Victoria Land Basin

## Introduction

In December 2007, the Antarctic Drilling (ANDRILL) program completed its second hole (AND-2A, Figure 1), recovering 98% of the sediments cored to a depth of 1,138.54 m below the sea floor (bsf) in McMurdo Sound (Florindo et al. 2008; Harwood et al. 2008). The fundamental goal of the ANDRILL program is to obtain from high-resolution sediment cores important new information about the Neogene Antarctic climate and evolution of Antarctic rift basins (<http://andrift.org/>). A focus of the Southern McMurdo Sound (SMS) project is to recover strata from the Middle Miocene, a period char-

acterized by warmer conditions (Middle Miocene Climatic Optimum) followed by long-term climate change towards cold-polar conditions (Flower and Kennett 1994; Zachos et al. 2001; Holbourn et al. 2007; Zachos et al. 2008). This objective was accomplished, providing an expanded Early to Middle Miocene record (Harwood et al. 2008) and filling the gap left by previous drilling of older sediments (~34–17 Ma) recovered in the Cape Roberts project (CRP in Figure 1–Barrett 2007) and younger sediments (~14–0 Ma) recovered in the first

ANDRILL hole (AND-1B, MIS in Figure 1) during the McMurdo Ice Shelf project (Naish et al. 2007).

All the objectives of the SMS project rely heavily on the achievement of an age model for the core that is as accurate as possible. This study reports the entire set of  $^{40}\text{Ar}$ – $^{39}\text{Ar}$  data available from volcanogenic products of the AND-2A core in conjunction with petro-chemical and lithological data of the dated materials, with a two-fold purpose: first, to examine possible correlations with the activity of the Erebus Volcanic Province in order to

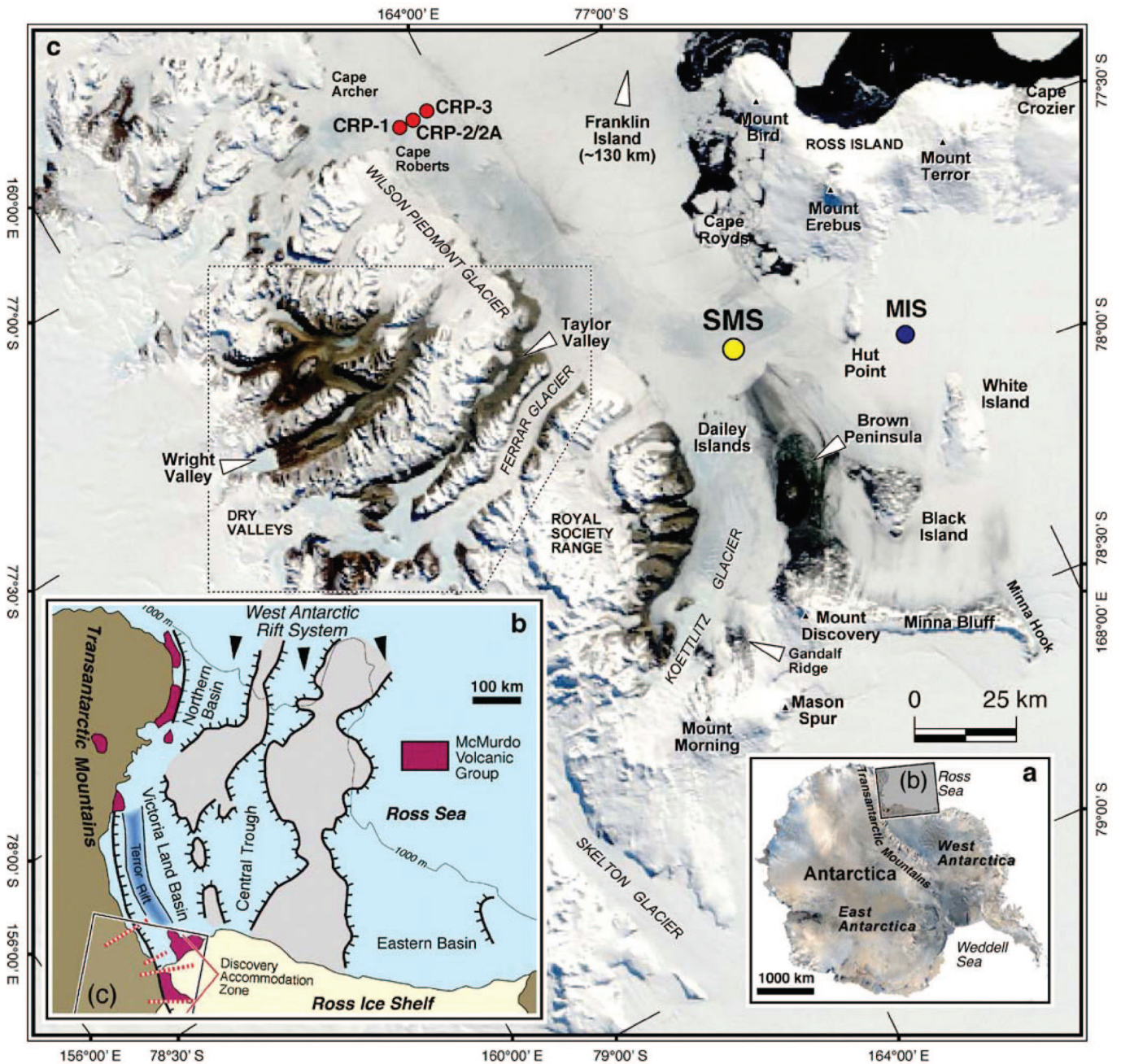


**Figure 1.** Satellite image of the McMurdo Sound area showing the location of the ANDRILL SMS (AND-2A) drill site and previous drill sites. *Inset b* has been redrawn and modified after Fielding et al. (2008a).

constrain possible volcanic sources; and second, to discuss the implications for the age model of the core and, more in general, for sedimentation in the Victoria Land Basin since Early Miocene.

## Background

### *The AND-2A core*

The AND-2A core contains terrigenous clastic lithologies ranging from claystones through siltstones and sandstones to conglomerates, breccias, and diamictites. The core is subdivided into 14 lithostratigraphic units on the basis of major changes in lithology with particular emphasis on diamictite abundance and associated sediments relative to other lithologies (Fielding et al. 2008b). Fielding et al. (2008b) identified 13 recurring lithofacies interpreted to represent a wide spectrum of depositional environments ranging from minimally ice-influenced, shallow marine settings (e.g., diatomite and fossil-rich mudstone), through ice contact proglacial and glacimarine (e.g., ripple cross-laminated sandstone, interlaminated sandstone, siltstone, and diamictite) to possibly subglacial environments (e.g., massive diamictite that shows extensive shear and rotation fabrics). The lithologies are arranged vertically in a repetitive fashion through the length of the core and are divided into 70 sequences, each of which fine upward and are truncated by the next sequence boundary (Fielding et al. 2008b). Each sequence possibly represents a cycle of maximum ice advance followed by a transgression towards minimum ice conditions (C. Fielding, personal communication, 2009).

Volcanic material is persistent throughout the AND-2A core and is the dominant clast type (>50%) in nine of the 14 lithostratigraphic units (Panter et al. 2008). Lithostratigraphic Unit 1 corresponds to the top 37 m of the core and is composed entirely of volcanoclastic sediments, including nearly primary tephra layers, clast-supported lava breccia, and ripple cross-laminated vitroclastic sands. This unit is interpreted to represent shallow marine to emergent volcanism from a previously unknown volcano close to the drill site (Del Carlo et al. 2009). Volcanic material within the other thirteen lithostratigraphic units consists mostly of lava clasts found in coarse grained deposits (e.g., conglomerate, diamictite) and rare, primary to moderately reworked, tephra layers that occur as thin accumulations within sandstones and siltstones in the lower half of the hole (Panter et al. 2008).

### *Volcanism in the McMurdo Sound area*

McMurdo Sound and the land surrounding it is an area with a rich history of rift-related alkaline vol-

canism. Large volcanoes include Mount Erebus (~2,000 km<sup>3</sup>), Mount Terror, and Mount Bird, which form Ross Island, Mount Discovery, Minna Bluff, and Mount Morning located on the mainland (Figure 1). These volcanoes as well as many smaller volcanic centers (e.g., Brown Peninsula, White and Black Islands) and volcanic fields (foothills of Royal Society Range, Wright-Taylor Valleys, Dailey Islands group) are part of the Erebus Volcanic Province of the McMurdo Volcanic Group (Kyle and Cole 1974; Kyle 1990a, b). The Erebus Volcanic Province represents the largest area of exposed Late Cenozoic volcanic rocks and the longest and most complete record of alkaline volcanism in Antarctica. The volcanic deposits on land range in age from approximately 19 Ma to current Strombolian-style activity within the summit crater of the Erebus Volcano (Dibble et al. 2008; Kelly et al. 2008). Evidence for older activity is from volcanoclastic sediments and tephra found in drill cores (CIROS-1, MSSTS-1, Cape Roberts, and AND-2A) and extends the history of alkaline volcanism in this area back to 26–20 Ma (Gamble et al. 1986; Barrett 1987; McIntosh 1998, 2000).

The volcanism is located in the southern portion of the Victoria Land Basin, one of four major rift-related basins within the Ross Sea (Figure 1b), which, along with the Transantarctic Mountains, are components of the West Antarctic rift system (Van der Wateren and Cloetingh 1999). Extension, rifting, and basin subsidence began in the Eocene to Early Oligocene (Fielding et al. 2008a). On the basis of drillhole and seismic reflection studies (Fielding et al. 2008a and references therein), the Victoria Land Basin evolved in a series of intervals each reflecting changes in basin forming tectonic processes. A phase of renewed rifting during the Middle to Late Miocene in the Southern Victoria Land Basin produced the Terror Rift (Wilson 1995, 1999; Fielding et al. 2008a). Volcanism in the Erebus Volcanic Province exploited structural weaknesses associated with the Terror Rift and Discovery Accommodation Zone (Figure 1b), a transverse boundary that segments the rift (Cooper et al. 1987; Wilson 1999; Johnston et al. 2008). Volcanic vents appear to be aligned along major normal faults and transverse lineaments with large volcanoes located at the intersection of these structures (Wilson 1999). There also appears to have been a broad shift in the main centers of volcanism from the continent, well within the accommodation zone (base of Mount Morning, Mason Spur), to the northeast into the center of the rift (i.e., Ross Island and Franklin Islands) beginning around 13 Ma. One interpretation of the structure or volcanic relationship is that a regional trans-tensional neotectonic regime controls the volcanic patterns and has formed stress-controlled linear fissure arrays and reactivated preexisting structures (Wilson 1999; Wilson and Demosthenous 2000; Wilson et al. 2003; Johnston et al. 2008). An alternative explanation involving mantle plumes

has also been proposed to explain the high volumes of evolved erupted material and the three-armed pattern of volcanism centered around Mount Erebus on Ross Island and Mount Discovery on the continent (Kyle 1990b; Kyle et al. 1992). The age and compositional data from volcanic materials recovered in the AND-2A core will be used to constrain the evolution of the Erebus Volcanic Province and, by virtue of their intimate association with the tectonic, sediment, and climate records, the factors that controlled its development.

The geochemistry of lava clasts and glass separated from tephra and volcanoclastic sediments indicates that all of the volcanic material in the AND-2A core is of alkaline affinity and the majority plots within the known compositional field of the Erebus Volcanic Province (Panter et al. 2008; Del Carlo et al. 2009). Lava clasts and glass from the core are compositionally diverse and include variably alkaline compositions (e.g., the *ne*-normative content of the lava clasts ranges from 0 to 16) that represent both moderately silica-undersaturated and highly silica-undersaturated alkaline magma lineages. In terms of evolutionary degree, both affinity lineages include primitive to weakly evolved samples (alkali basalt and basanite, respectively) along with strongly evolved ones (trachyte and phonolite, respectively). It is noteworthy that the most evolved samples (trachyte and rhyolite) from the moderately alkaline lineage have a peralkaline chemical signature that is only found at Mount Morning (Kyle 1990a). Finally, the whole rock clasts and glass shard compositions from AND-2A core display a very limited overlap with the volcanic glasses from the McMurdo Ice Shelf project (MIS, Figure 1) AND-1B core (Pompilio et al. 2007). This distinction might indicate an important spatial and temporal change in the chemical evolution of the volcanic activity in the region.

#### **<sup>40</sup>Ar–<sup>39</sup>Ar data: results and interpretation**

In this section, we report and interpret <sup>40</sup>Ar–<sup>39</sup>Ar data for a subset of 17 samples, consisting of clasts and primary to moderately reworked tephra layers. These samples were selected after careful examination of 33 specimens, initially selected for dating on the basis of on-ice descriptions (Fielding et al. 2008b; Panter et al. 2008). Nine out of the 14 identified lithostratigraphic units (i.e., 1, 4, 7, 8, 9, 10, 11, 12, and 14) contained suitable materials for dating, consisting of volcanic lava clasts or pumice-rich layers. In contrast, within the remaining five lithostratigraphic units (i.e., 2, 3, 5, 6, and 13) datable volcanogenic products were not found. The main features of selected samples along with the degree of reworking are summarized in Table 1. More details on the petrographic features, along with the analytical procedures and full <sup>40</sup>Ar–<sup>39</sup>Ar data, are given in the Supple-

mentary Material. Ages were calculated using the IUGS recommended constants (Steiger and Jäger 1977), in order to allow direct comparison with previously published Ar data. However, in “Discussion” section, we examine the effects in the calculated ages of the recently recognized problems in the <sup>40</sup>K decay constants (e.g., Min et al. 2000; Schoene et al. 2006) and of the possible solution proposed by Kuiper et al. (2008).

#### ***Lithostratigraphic Unit 1 (0–37.01 m bsf)***

Phonolite clast 8.88–9.02 m bsf represents the uppermost sample analyzed of the whole set (Table 1). The large-sized alkali feldspar crystals (up to a few centimeters) were crushed and sieved to the 300–500 μm grain size in order to facilitate the removal of melt inclusions during the leaching procedure. After leaching, however, several grains still preserved numerous internal melt inclusions. Sample was first analyzed by the <sup>40</sup>Ar–<sup>39</sup>Ar total fusion technique applied to milligram-sized splits (see Table S1 in the ESM). Four total fusion analyses gave apparent ages overlapping within analytical errors, with an error-weighted mean age of  $0.124 \pm 0.014$  Ma ( $\pm 2\sigma$  internal error), a mean square of weighted deviates (MSWD) of 0.59 and a constant K/Ca ratio (Figure 2). In an <sup>36</sup>Ar/<sup>40</sup>Ar vs. <sup>39</sup>Ar<sub>K</sub>/<sup>40</sup>Ar isochron plot (not shown), data are poorly scattered and define a slightly younger intercept age of  $0.107 \pm 0.039$  Ma ( $\pm 2\sigma$  internal error, MSWD = 0.89) and an initial <sup>40</sup>Ar/<sup>36</sup>Ar ratio of  $301 \pm 11$ , within error with that of modern atmospheric Ar (<sup>40</sup>Ar/<sup>36</sup>Ar = 295.5). A step-heating run on the same mineral concentrate was performed in order to verify the behavior of the sample when subjected to incremental heating. Alkali feldspar 8.88–9.02 m bsf yielded a discordant hump-shaped age profile (Figure 3), with apparent ages ranging from  $0.053 \pm 0.022$  to  $0.220 \pm 0.026$  Ma ( $\pm 2\sigma$  analytical errors), attesting to sample heterogeneity not revealed by total fusion analysis. The total gas apparent age from step-heating data is  $0.127 \pm 0.012$  Ma ( $\pm 2\sigma$  analytical error) and closely matches those from total fusion data. An <sup>40</sup>Ar\*/<sup>39</sup>Ar<sub>K</sub> vs. <sup>38</sup>Ar<sub>Cl</sub>/<sup>39</sup>Ar<sub>K</sub> three-isotope correlation diagram (converted to age and Cl/K ratio—Figure 4) of data from both total fusion and step-heating analyses reveals a fairly well-defined positive correlation for the whole dataset, suggesting that the system is dominated by binary mixing between two end-members: (1) a high <sup>40</sup>Ar\*/<sup>39</sup>Ar<sub>K</sub> and Cl/K component and (2) a component with a lower <sup>40</sup>Ar\*/<sup>39</sup>Ar<sub>K</sub> ratio and a Cl/K ratio close to zero. A similar positive correlation has been documented for alkali feldspar phenocrysts from Mount Erebus and assigned to trapped excess argon (i.e., parentless <sup>40</sup>Ar) hosted in melt inclusions along with Cl within the alkali feldspar (Esser et al. 1997). Taking into account that the alkali feldspar does not accommodate Cl in its crystal lattice and assuming that the

**Table 1.** Samples from the AND-2A core analyzed by the  $^{40}\text{Ar}$ – $^{39}\text{Ar}$  dating method

Sample (depth interval in m bsf)	LSU	Type	Lithology	Deposit type	Degree of reworking	Phase analyzed
8.88–9.02 <sup>a</sup>	1.1	Lava clast	Phonolite <sup>b</sup>	Bagged sample <sup>d</sup>	Strongly reworked	Alkali feldspar
10.22–10.44	1.2	Lava clast	Basanite <sup>b</sup>	Bagged sample <sup>d</sup>	Strongly reworked	Groundmass
12.23–12.41	1.2	Lava clast	Hawaiite <sup>b</sup>	Bagged sample <sup>d</sup>	Strongly reworked	Groundmass
18.03–18.25	1.2	Lava clast	Hawaiite <sup>b</sup>	Bagged sample <sup>d</sup>	Strongly reworked	Groundmass
18.69–18.73	1.2	Lava clast	Tephrite <sup>b</sup>	Bagged sample <sup>d</sup>	Strongly reworked	Groundmass
127.50–127.52	4	Lava clast	Felsic <sup>c</sup>	Diamictite	Strongly reworked	Alkali feldspar
129.96–129.97	4	Lava clast	Basaltic <sup>c</sup>	Diamictite	Strongly reworked	Plagioclase
358.11–358.13	7	Lava clast	Intermediate <sup>c</sup>	Diamictite	Strongly reworked	Groundmass
440.83–440.86	8.1	Lava clast	Intermediate <sup>c</sup>	Mudstone	Strongly reworked	Alkali feldspar
564.92–564.93	8.2	Lava clast	Felsic <sup>c</sup>	Conglomerate	Strongly reworked	Alkali feldspar
640.13–640.16	9	Pumice	Felsic <sup>c</sup>	Lapilli tuff	Primary	Alkali feldspar
709.14–709.16	10	Pumice	Felsic <sup>c</sup>	Tuffaceous sandstone	Moderately reworked	Alkali feldspar
709.17–709.19	10	Pumice	Felsic <sup>c</sup>	Tuffaceous sandstone	Moderately reworked	Alkali feldspar
831.66–831.68	11	Pumice	Felsic <sup>c</sup>	Tuffaceous silty-sandstone	Nearly primary	Alkali feldspar
953.28–953.31	12	Pumice	Felsic <sup>c</sup>	Tuffaceous fine muddy sandstone	Nearly primary	Alkali feldspar
953.54–953.56	12	Pumice	Felsic <sup>c</sup>	Tuffaceous fine muddy sandstone	Nearly primary	Alkali feldspar
1093.00–1093.04	14	Pumice	Felsic <sup>c</sup>	Tuffaceous sandstone	Nearly primary	Alkali feldspar

LSU = lithostratigraphic unit

a. Sample 8.88–9.02 corresponds to sample 8.88–9.02a in Del Carlo et al. (2009)

b. Lithology determined from whole-rock geochemistry (see Del Carlo et al. 2009)

c. Lithology determined from mineralogy/mineral chemistry

d. Stratigraphic relationships not recognizable

system consists of a simple binary mixture (i.e., alkali feldspar with no excess Ar and Cl and melt inclusions with both excess Ar and Cl), then the true Ar age should be defined in Figure 4 by the extrapolation of the trend to the  $y$ -axis at a Cl/K ratio of zero. A least-squares fit for the whole dataset yields a  $y$ -intercept age of  $0.035 \pm 0.045$  Ma and a MSWD of 2.0 (Figure 4), attesting to a slight excess of scatter exceeding analytical uncertainties (probability of fit 0.021). Excluding step no. 3 (Figure 4), we obtain a comparable but more precise intercept age of  $0.057 \pm 0.023$  Ma and a statistically acceptable MSWD of 0.93 (probability of fit 0.51). In light of the above arguments, we conservatively interpret Ar data from alkali feldspar 8.88–9.02 to indicate an eruption age  $\leq 0.080$  Ma for the phonolite.

The groundmass of the basanite lava clast from the 10.22–10.44 m bsf interval, yielded an internally discordant age spectrum with a descending shape and a total gas apparent age of  $0.662 \pm 0.042$  Ma ( $\pm 2\sigma$  interval error). Similar age spectra are common for volcanic groundmass and are explained by loss and/or redistribution of neutron-produced  $^{39}\text{Ar}_K$  and  $^{37}\text{Ar}_{Ca}$  during sample irradiation (e.g., Koppers et al. 2000). Four consecutive steps from the intermediate-temperature region, representing  $\sim 60\%$  of the total  $^{39}\text{Ar}_K$  released, define a

concordant segment (MSWD = 0.59) yielding an error-weighted mean age of  $0.692 \pm 0.038$  Ma ( $\pm 2\sigma$  internal error). This age matches the intercept age of  $\sim 0.691$  Ma derived from isochron analysis of the four steps in a  $^{36}\text{Ar}/^{40}\text{Ar}$  vs.  $^{39}\text{Ar}_K/^{40}\text{Ar}$  plot (initial  $^{40}\text{Ar}/^{36}\text{Ar}$  ratio of  $295.7 \pm 5.5$ ). The weighted mean age of  $0.692 \pm 0.038$  Ma overlaps within analytical errors with the total gas age and is taken as the eruption age of the basanitic lava.

The hawaiite clast from the 12.23–12.41-m bsf interval yielded a comparable shaped age profile as the previous sample, though a significant concordant segment is not defined (Figure 3). However, two consecutive steps (representing  $\sim 33\%$  of the total  $^{39}\text{Ar}_K$  released), characterized by the highest radiogenic Ar contents and comparable Ca/K ratios (nos. 3 and 4, Table S1 in the ESM), overlap within errors and yield a weighted mean age of  $0.793 \pm 0.063$  Ma ( $\pm 2\sigma$  internal error), in close agreement with the total gas age ( $0.758 \pm 0.090$  Ma). The  $0.793 \pm 0.063$ -Ma is taken as the best age constraint derivable for clast 12.23–12.41 m bsf.

Two other mafic lava clasts were examined from the Lithostratigraphic Unit 1 but yielded anomalously old preliminary total fusion ages of  $16.1 \pm 2.2$  and  $9.5 \pm 1.2$  Ma (sample 18.03–18.25 and 18.69–18.73 m bsf, respectively; Table S1 in the ESM), that although affected

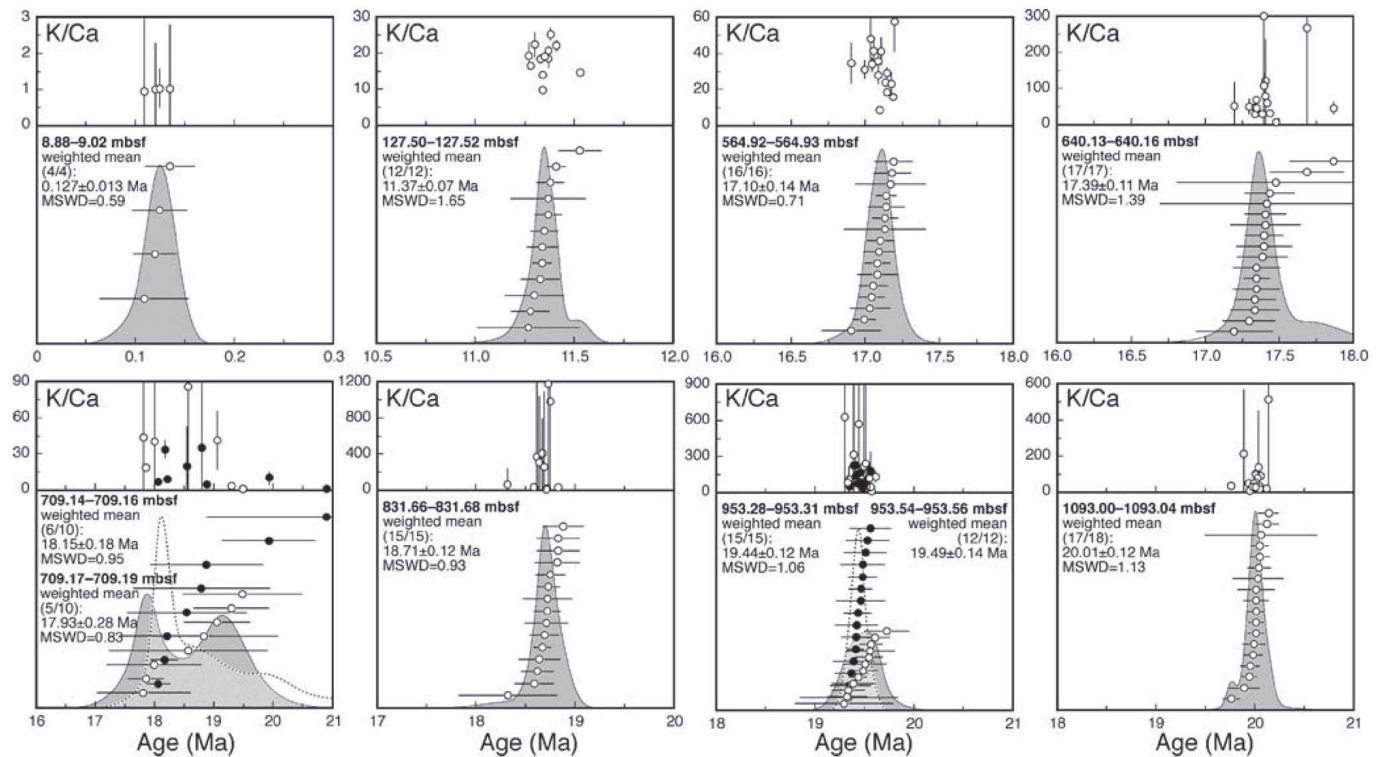


**Figure 2.** Cumulative probability and ranked distribution of ages from total fusion experiments on alkali feldspar separates. Bars are  $2\sigma$  analytical errors. Uncertainties on the error-weighted mean ages also include the error in the  $J$  values.

by large uncertainties, suggest that clasts were transported and reworked long before they were deposited at the level of sampling. Given the much older age than those reasonably expected for sediments at 18–19 m bsf, step-heating experiments on these two samples were not completed.

#### *Lithostratigraphic Unit 4 (122.86–224.82 m bsf)*

A felsic lava clast from the 127.50–127.52-m bsf interval was analyzed by the  $^{40}\text{Ar}$ – $^{39}\text{Ar}$  total fusion technique on single to a few alkali feldspar grains. The whole set of data (12 analyses, Table S1 in the ESM) gives in a cumulative probability plot (Figure 2) a nearly single-mode distribution, typical of within-sample homogeneity of data. The error-weighted mean of the 12 total fusion analyses is  $11.369 \pm 0.074$  Ma ( $\pm 2\sigma$  internal error), MSWD 1.6 and probability of fit only 0.078. Analyses no. 9, along with 7 and 8 (Table S1 in the ESM), were obtained from a single millimeter-sized alkali feldspar phenocryst, which may be potentially affected by the presence of inherited Ar due to a protracted crystallization history, as demonstrated for volcanic rocks from other areas (e.g., Bachmann et al. 2007). Omitting analysis no. 9, which gave the most (oldest) discordant age, then the error-weighted mean is  $11.363 \pm 0.072$  Ma ( $\pm 2\sigma$

internal error), the MSWD 1.00 and the probability of fit 0.44. This age is taken as the best age estimate for the felsic lava.

In the slightly deeper 129.96–129.97 m bsf interval of Lithostratigraphic Unit 4, a plagioclase separate from a basaltic clast was analyzed by the step-heating technique. A split of a few tens of milligrams of plagioclase separate was incrementally heated until fusion over eight steps and yielded an internally concordant age profile (Figure 3). The first three steps are characterized by a low to very low radiogenic Ar contents (down to 0.1%) and, consequently, are affected by large analytical errors. However, steps 4 to 8 display much lower atmospheric Ar contents ( $^{40}\text{Ar}^*$  contents up to ~60%, Table S1 in the ESM) and yield smaller analytical errors. The error-weighted mean age calculated using all steps is  $11.43 \pm 0.46$  Ma ( $\pm 2\sigma$  internal error, MSWD = 0.71), within error with the isochron age of  $11.39 \pm 0.49$  (initial  $^{40}\text{Ar}/^{36}\text{Ar}$  ratio of  $296.0 \pm 2.3$ ) and is, therefore, statistically indistinguishable from the age of clast 127.50–127.52.

#### *Lithostratigraphic Unit 7 (339.92–436.18 m bsf)*

In the Lithostratigraphic Unit 7, only an intermediate lava clast, collected from the 358.11–358.13-m bsf interval, was investigated and analyzed by the laser step-

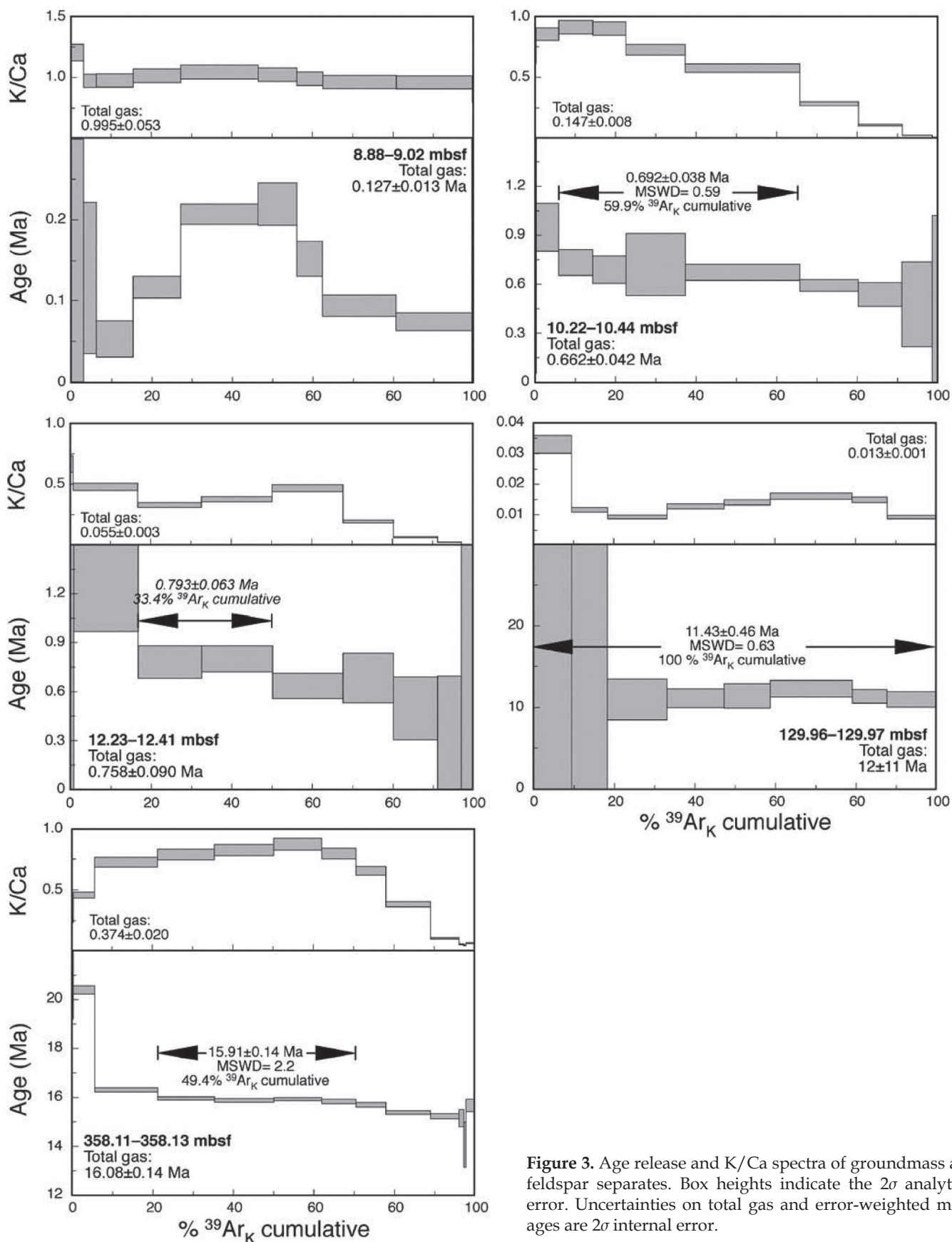


**Figure 3.** Age release and K/Ca spectra of groundmass and feldspar separates. Box heights indicate the  $2\sigma$  analytical error. Uncertainties on total gas and error-weighted mean ages are  $2\sigma$  internal error.



heating extraction technique on a few tens of milligrams of groundmass separate. The age spectrum compares in shape with those of groundmasses from the Lithostratigraphic Unit 1 (Figure 3); yet, data are much more precise due to the comparatively much higher radiogenic Ar contents (Table S1 in the ESM). Four consecutive steps from the intermediate temperature region, characterized by the highest radiogenic Ar contents, similar K/Ca ratios, and representing together ~50% of the total  $^{39}\text{Ar}_K$  released, define a concordant segment (MSWD = 2.2, probability of fit 0.083) yielding an error-weighted mean age of  $15.91 \pm 0.14$  Ma. This date overlaps within error limits with the less precise intercept age of  $15.74 \pm 0.29$  Ma ( $\pm 2\sigma$  analytical error) from isochron analysis and is considered a reliable eruption age.

#### *Lithostratigraphic Unit 8 (436.18–608.35)*

The intermediate lava clast from the 440.83–440.86-m bsf interval gave a poor alkali feldspar crystal yield, which, under a stereomicroscope, appeared to be contaminated by rounded quartz and plagioclase. Total fusion analyses were attempted on single feldspar grains and yielded a wide range of ages, from  $16.23 \pm 0.77$  to ~700 Ma thus attesting to contamination of the mineral concentrate by grains derived from the crystalline basement. The two youngest total fusion analyses match within errors, and gave an error-weighted mean age of  $16.54 \pm 0.34$  Ma. This age, yet quite imprecise, represents a maximum age estimate for the time of deposition at the 440.83–440.86-m bsf interval.

Mineral separation from a felsic lava clast of the same lithostratigraphic unit, from the 564.92–564.93-m bsf interval, gave euhedral alkali feldspar, some of which sufficiently large to be analyzed by single-grain total fusion analysis. Seven out of 16 runs were completed on single grains and the remaining on a few grains (3 to 5, Table S1 in the ESM). The whole set of data, when plotted in a cumulative probability distribution diagram, exhibits a well-defined single-mode distribution attesting to homogeneity of data. The error-weighted mean age for the 16 analyses is  $17.10 \pm 0.14$  Ma and is taken as the age of the felsic lava.

#### *Lithostratigraphic Unit 9 (607.35–648.74 m bsf)*

From Lithostratigraphic Unit 9 down hole, studied samples consist of primary to moderately reworked tephra-rich layer thus providing the most robust age determinations for the whole AND-2A core.  $^{40}\text{Ar}$ – $^{39}\text{Ar}$  age data were performed using the total fusion technique, whenever possible, on single crystals. When crystals were too small to yield reasonably precise age determinations, total fusion analyses were performed on multigrain splits. Numbers of crystals used in each run are listed in Table S1 in the ESM.

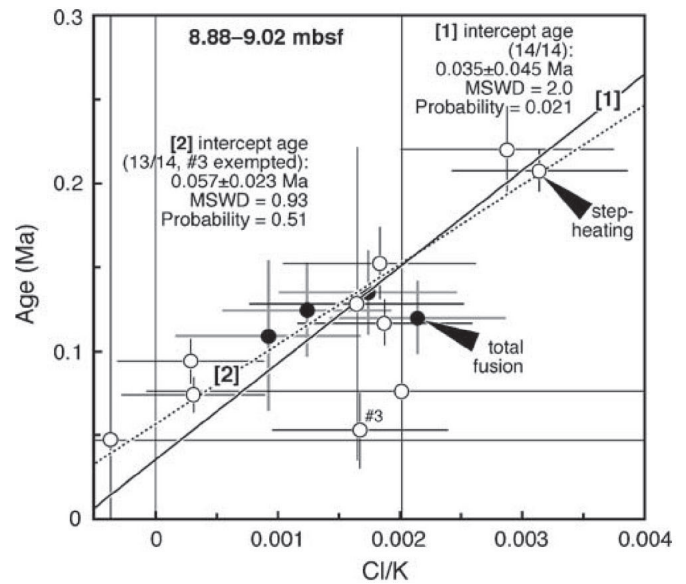


**Figure 4.** Age (Ma) vs. Cl/K (derived from neutron-produced  $^{38}\text{Ar}_{\text{Cl}}/^{39}\text{Ar}_K$  ratios) diagram for data from step-heating and total fusion analyses on alkali feldspar of clast 8.88–9.02. Note the well-defined positive correlation suggesting that the spread of data can be accounted for by a binary mixture.

Mineral separation on the 640.13–640.16 tephra layer gave mostly euhedral to subhedral alkali feldspar grains which however were not large enough for single-grain analyses. Total fusion experiments were, therefore, chiefly performed on splits consisting of a few crystals that, in a cumulative probability distribution plot (Figure 2), yield a single-mode distribution and an error-weighted mean age of  $17.39 \pm 0.11$  Ma ( $\pm 2\sigma$  internal error, MSWD = 1.4 and probability of fit 0.14). A least squares fit in a  $^{36}\text{Ar}/^{40}\text{Ar}$  vs.  $^{39}\text{Ar}_K/^{40}\text{Ar}$  isochron diagram (Figure 5) through the 17 data points yields a nominally younger age of  $17.302 \pm 0.069$  Ma ( $\pm 2\sigma$  analytical error) and an initial  $^{40}\text{Ar}/^{36}\text{Ar}$  ratio of  $360 \pm 39$ , significantly higher than that of modern atmospheric Ar. This in principle indicates that alkali feldspar 640.13–640.16 may be slightly contaminated by excess Ar thereby suggesting that the best age estimate for the tephra should be that derived from isochron analysis. However, close inspection of Figure 5 reveals that the slope of the regression line is strongly dependent on one data point (analysis no. 11), which is characterized by the lowest radiogenic Ar content (Table S1 in the ESM). Excluding this analysis from the regression calculation then the  $y$ -intercept becomes indistinguishable at the  $2\sigma$  confidence level ( $362 \pm 76$ ) from that of modern atmospheric Ar and the  $x$ -intercept age  $17.300 \pm 0.099$  Ma ( $\pm 2\sigma$  analytical error), is well within  $1\sigma$  error with the error-weighted mean age. The latter is taken as the age of alkali feldspar, and given the primary character of the tephra

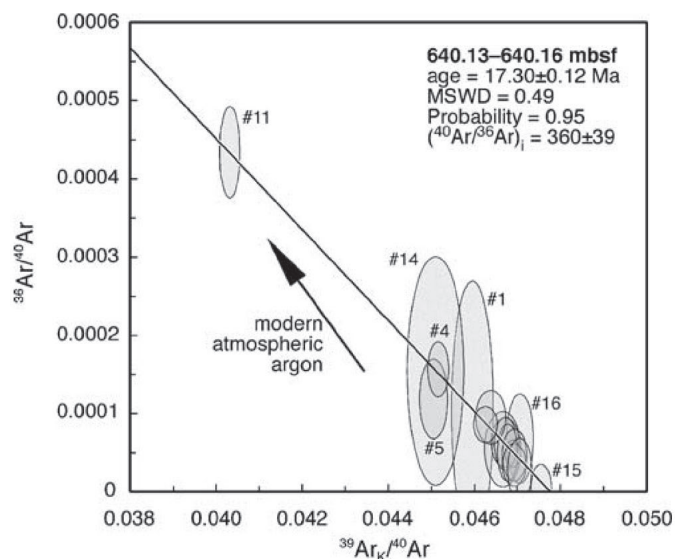


**Figure 5.** Isochron plot ( $^{36}\text{Ar}/^{40}\text{Ar}$  vs.  $^{39}\text{Ar}/^{40}\text{Ar}$  three-isotope correlation diagram) for total fusion analyses on alkali feldspar from tephra layer 640.13–640.16

layer, the  $17.39 \pm 0.11$ -Ma age represents a meaningful estimate for depositional age of the 640.13–640.16-m bsf interval.

#### *Lithostratigraphic Unit 10 (648.74–778.34 m bsf)*

The two pumice layers from the 709.14 to 709.19-m bsf interval (samples, 709.14–709.16 and 709.17–709.19) yielded alkali feldspar crystals insufficiently large ( $\ll 1$  mm in length) for single-grain total fusion analyses. Furthermore, mineral concentrate from both samples contained anhedral plagioclase and rounded quartz grains that, in agreement with petrographic results (see ESM), indicate the presence of an older detrital component. Multigrain splits from sample 709.14–709.16 yielded a wide range of age from  $\sim 18.1$  to  $\sim 240$  Ma (Figure 2 and Table S1 in the ESM). However, six out of ten analyses yielded the youngest ages and a statistically acceptable error-weighted mean of  $18.15 \pm 0.18$  Ma ( $\pm 2\sigma$  internal error, MSWD = 0.95, probability of fit 0.45). Similarly, sample 709.17–709.19 gave a wide range of apparent ages (Figure 2 and Table S1 in the ESM). Younger ages are in line with the mean age of sample 709.14–709.16, but the remaining data yield older apparent ages (up to  $\sim 100$  Ma) associated to higher Ca/K ratios (Table S1 in the ESM) and indicating contamination by older detrital plagioclase. The younger five out of ten analyses gave an error-weighted mean age of  $17.93 \pm 0.28$  Ma (MSWD = 0.83) that is indistinguishable at the

$1\sigma$  confidence level from the mean age of sample 709.14–709.16 m bsf. The  $\sim 18$ -Ma age is, therefore, taken as a close approximation of the time of deposition of sediments at 709.14 to 709.19-m bsf interval.

#### *Lithostratigraphic Unit 11 (778.34–904.66 m bsf)*

The pumice concentration from the 831.66–831.68-m bsf interval yielded a crystal separate characterized by mostly millimeter-sized euhedral grains. Eleven out of 15  $^{40}\text{Ar}$ - $^{39}\text{Ar}$  runs were completed on single grains and the remaining analyses on splits consisting of three grains. The whole dataset defines in a cumulative probability plot a single-mode distribution and an error-weighted mean age of  $18.71 \pm 0.12$  ( $\pm 2\sigma$  internal error, MSWD = 0.93, probability of 0.53), well distinguishable at the  $2\sigma$  confidence level from the mean age of the previous sample. Given the nearly primary character of this tephra layer, the mean age of alkali feldspar is taken as the depositional age of the 831.66–831.68-m bsf interval.

#### *Lithostratigraphic Unit 12 (904.66–996.69 m bsf)*

Alkali feldspar separates from both samples (953.28–953.31 and 953.54–953.56) of the 953.28–953.56-m bsf interval, consist of euhedral grains, which were mainly analyzed by total fusion analyses on single crystals and gave intrasample concordant ages within analytical errors (Figure 2). Error-weighted mean ages are  $19.44 \pm 0.12$  Ma ( $\pm 2\sigma$  internal error, MSWD = 1.06, probability 0.39) and  $19.49 \pm 0.14$  Ma ( $\pm 2\sigma$  internal error, MSWD = 1.11, probability 0.35) for sample 953.28–953.31 and 953.54–953.56, respectively, and are, therefore, indistinguishable at the  $1\sigma$  confidence level. These ages represent a reliable estimate for the depositional age of the 953.28–953.56-m bsf interval.

#### *Lithostratigraphic Unit 14 (1,040.28–1,138.54)*

Tephra layer 1,093.00–1,093.04 represents the deepest sample investigated and comes from less than 50 m from the bottom of the AND-2A core (1,138.54 m bsf). The mineral concentrate consisted of euhedral millimeter-sized alkali feldspar grains. Eighteen single-grain total fusion analyses yielded an error-weighted mean with a probability of fit  $\ll 0.05$ , attesting to an excess of scatter exceeding analytical uncertainties and indicating intrasample heterogeneity (Figure 2 and Table S1 in the ESM). However, the excess of scatter is due to only one analysis (no. 9, Table S1 in the ESM). If this run is taken as an outlier and is omitted from the weighted mean calculation, then the probability of fit is 0.32, with an error-weighted mean age of  $20.01 \pm 0.12$  Ma. This age is again statistically distinguishable from those of the previous samples and is considered a reliable estimate of depositional age at the 1,093.00–1,093.04-m bsf interval.

## Discussion

### *Influence of the “inaccuracy” of $^{40}\text{K}$ decay constants*

$^{40}\text{Ar}$ - $^{39}\text{Ar}$  geochronological data presented above have yielded 10 statistically robust age determinations, five of which directly constraining the time of deposition at the level of sampling. Possible volcanic sources and the implications for the age model of the core and, more generally for the time, rate, and nature of sediment deposition in the Victoria Land Basin since Early Miocene, are discussed in the specific sections below. Age data obtained in the present study are summarized in Table 2 and have been calculated using both the IUGS recommended  $^{40}\text{K}$  decay constants (Steiger and Jäger 1977), along with an age of 28.03 Ma for the FCs standard (Jourdan and Renne 2007) and the more realistic constants recently proposed by Kuiper et al. (2008).

It is important to recall here that the  $^{40}\text{Ar}$ - $^{39}\text{Ar}$  method is inherently a relative technique in that ages are calibrated against those of neutron-fluence monitors (dating standards) and calculated using available  $^{40}\text{K}$  decay constants. This implies that the accuracy of a  $^{40}\text{Ar}$ - $^{39}\text{Ar}$  age is limited by the accuracy of primary standards as well as by the precision and accuracy of intercalibrations among standards and of the  $^{40}\text{K}$  decay constants (e.g., Renne et al. 1998). This is a critical issue because whenever Ar ages are used in “absolute” sense or are compared to age data derived from other radioisotopic or non-radioisotopic techniques, the uncertainty in age should include all known sources of error, including those associated to the calibration of the fluence monitor and of  $^{40}\text{K}$  decay constants. If on the one hand the uncertainty on the calibration of the FCs dating standard against primary standards (age based on  $^{40}\text{Ar}^*$  determined by “first principle”) has been recently and significantly improved (Jourdan and Renne 2007), on the other hand, the  $^{40}\text{K}$  decay constants are currently under scrutiny, particularly the  $^{40}\text{K}$  branching ratio. At present, most of the uncertainty associated to a  $^{40}\text{Ar}$ - $^{39}\text{Ar}$  age, when all sources of systematic errors are considered, is indeed due to uncertainties in radioactive decay rates (e.g., Renne et al. 1998). The basis for the  $^{40}\text{K}$  decay constants in current use by geochronologists was discussed in detail by Min et al. (2000), who noted that the  $^{40}\text{K}$  decay constants used in geochronology since 1977 (Steiger and Jäger 1977) are quite different from those used by the nuclear physics community and concluded that the total  $^{40}\text{K}$  decay constant is known to no better than  $\pm 2\%$  ( $2\sigma$  level). The detrimental effect of the uncertainties in  $^{40}\text{K}$  decay constants on a  $^{40}\text{Ar}$ - $^{39}\text{Ar}$  age is evident from Table 2: internal errors as low as 0.6–0.7% (e.g., samples 127.50–127.52 or 1,093.00–1,093.04) become as large as 1.7–1.8% when individual errors also include uncertainties in the  $^{40}\text{K}$  decay constants.

The lack of accuracy in the currently used  $^{40}\text{K}$  decay constants is confirmed by the growing body of data from rapidly cooled rocks indicating that  $^{40}\text{Ar}$ - $^{39}\text{Ar}$  ages tend to be systematically  $\leq 1\%$  younger than U-Pb ages (e.g., Min et al. 2000; Krumrei et al. 2006; Schoene et al. 2006). Since U decay constants are the most accurately known, reconciliation of  $^{40}\text{Ar}$ - $^{39}\text{Ar}$  and U-Pb ages requires that either the age of the  $^{40}\text{Ar}$ - $^{39}\text{Ar}$  standard is older, or the total  $^{40}\text{K}$  decay constant is smaller (Min et al. 2000). A possible solution to this problem has been recently proposed by Kuiper et al. (2008), who, comparing astronomical and  $^{40}\text{Ar}$ - $^{39}\text{Ar}$  ages of tephra in marine deposits and, assuming a more realistic total  $^{40}\text{K}$  decay constant of  $(5.463 \pm 0.214) \cdot 10^{-10} \text{ a}^{-1}$  (Min et al. 2000), obtained an age for FCs of  $28.201 \pm 0.046 \text{ Ma}$  ( $\pm 2\sigma$ , incorporating all sources of error), that is 0.65% older and over six times more precise than the most recently calibrated age against primary standards (Jourdan and Renne 2007). More significantly, the age of the standard proposed by Kuiper et al. (2008) was evaluated independently from the  $^{40}\text{K}$  decay constants, with the implication that the calculation of the age for an unknown sample calibrated against the FCs monitor only involves the  $^{40}\text{K}$  total decay constant, and consequently, it is nearly insensitive to the value adopted and to its uncertainty (Kuiper et al. 2008). As an example (see Table 2), using a total  $^{40}\text{K}$  decay constant of  $(5.463 \pm 0.214) \cdot 10^{-10} \text{ a}^{-1}$  (Min et al. 2000) and an age of  $28.201 \pm 0.046 \text{ Ma}$  (Kuiper et al. 2008) for FCs, we obtain for sample 127.50–127.52 an error-weighted mean age of  $11.432 \pm 0.091 \text{ Ma}$ , which becomes  $11.433 \pm 0.091 \text{ Ma}$  when the calculation assumes a total  $^{40}\text{K}$  decay constant of  $5.543 \pm 0.020 \cdot 10^{-10} \text{ a}^{-1}$  (Steiger and Jäger 1977).

### *Correlation with the Erebus Volcanic Province and possible volcanic sources*

The geochronological data based on available K-Ar and  $^{40}\text{Ar}$ - $^{39}\text{Ar}$  analyses on whole rocks, groundmasses, or mineral separates from volcanic rock samples of the Erebus Volcanic Province are summarized in Figure 6a–d and compared with  $^{40}\text{Ar}$ - $^{39}\text{Ar}$  ages from this work and from previous drill cores (Figure 6e). Age data quoted in this section and shown in Figure 6 were all calculated using the IUGS recommended  $^{40}\text{K}$  decay constants (Steiger and Jäger 1977) in order to be consistent with previously published Ar data. Errors on  $^{40}\text{Ar}$ - $^{39}\text{Ar}$  ages are given as  $2\sigma$  internal uncertainties and ages are consistent with the up-to-date age of the FCs monitor (see caption of Figure 6). Errors on K-Ar ages are those originally reported by the authors.

Figure 6 shows that the volcanic activity in the area was nearly continuous since Early Miocene and progressively propagated toward northeast, with ages of

**Table 2.** Summary of <sup>40</sup>Ar–<sup>39</sup>Ar results from samples of the AND-2A core

Sample (m bsf)	Phase analyzed	Extraction technique	Total number of analyses	Age (Ma) <sup>a</sup>	±2σ <sup>b</sup>	±2σ <sup>c</sup>	Type	MSWD	P value	Number of analyses	Age (Ma) <sup>d</sup>	±2σ <sup>e</sup>	Ages from polarity chron boundaries <sup>f</sup>	Ages from polarity chron boundaries <sup>g</sup>
8.88–9.02	Alkali feldspar	SH and TF (CO <sub>2</sub> laser)	14	≤0.080	–	–	3-isotope correlation diagram	–	–	14	≤0.080	–	–	–
10.22–10.44	Groundmass	SH (Nd:YAG laser)	10	0.692	0.038	0.040	EWM	0.59	0.62	4	0.696	0.038	0.040	–
12.23–12.41	Groundmass	SH (Nd:YAG laser)	10	0.793	0.063	0.066	EWM	0.10	0.75	2	0.798	0.063	0.065	–
18.03–18.25	Groundmass	TF (Nd:YAG laser)	1	16.1	2.2	2.2	TF	–	–	1	16.2	2.2	2.2	–
18.69–18.73	Groundmass	TF (Nd:YAG laser)	1	9.5	1.2	1.2	TF	–	–	1	9.6	1.2	1.2	–
127.50–127.52	Alkali feldspar	TF (CO <sub>2</sub> laser)	12	11.363	0.072	0.20	EWM	1.00	0.44	11	11.432	0.072	0.091	–
129.96–129.97	Plagioclase	SH (CO <sub>2</sub> laser)	8	11.43	0.46	0.50	EWM	0.63	0.73	8	11.50	0.46	0.48	–
358.11–358.13	Groundmass	SH (Nd:YAG laser)	13	15.91	0.14	0.29	EWM	2.2	0.083	4	16.01	0.14	0.17	15.85
440.83–440.86	Alkali feldspar	TF (CO <sub>2</sub> laser)	5	16.54	0.34	0.43	EWM	0.74	0.39	2	16.64	0.34	0.37	16.48
564.92–564.93	Alkali feldspar	TF (CO <sub>2</sub> laser)	16	17.10	0.14	0.31	EWM	1.4	0.15	16	17.20	0.14	0.17	17.14
640.13–640.16	Alkali feldspar	TF (CO <sub>2</sub> laser)	17	17.39	0.11	0.30	EWM	1.4	0.14	17	17.50	0.11	0.14	17.36
709.14–709.16	Alkali feldspar	TF (CO <sub>2</sub> laser)	10	18.15	0.18	0.34	EWM	0.95	0.45	6	18.26	0.18	0.21	17.50
709.17–709.19	Alkali feldspar	TF (CO <sub>2</sub> laser)	10	17.93	0.28	0.40	EWM	0.83	0.51	5	18.04	0.28	0.31	17.50
831.66–831.68	Alkali feldspar	TF (CO <sub>2</sub> laser)	15	18.71	0.12	0.33	EWM	0.93	0.53	15	18.82	0.12	0.15	18.18
953.28–953.31	Alkali feldspar	TF (CO <sub>2</sub> laser)	15	19.44	0.12	0.34	EWM	1.06	0.39	15	19.56	0.12	0.15	18.51
953.54–953.56	Alkali feldspar	TF (CO <sub>2</sub> laser)	12	19.49	0.14	0.34	EWM	1.11	0.35	12	19.61	0.14	0.17	18.51
1093.00–1093.04	Alkali feldspar	TF (CO <sub>2</sub> laser)	18	20.01	0.12	0.35	EWM	1.13	0.32	17	20.13	0.12	0.15	<20.16

Analytical procedures are described in the Supplementary Material.

P = probability of fit, SH = step-heating analysis, TF = total fusion analysis, EWM = error-weighted mean

a. Ages calculated using the IUGS recommended constants (Steiger and Jäger 1977) and an age of 28.03 Ma for the fluence monitor FCs (Jourdan and Renne 2007)

b. ±2σ internal error

c. ±2σ full error

d. Ages calculated using a <sup>40</sup>K total decay constants of (5.463 ± 0.214) × 10<sup>-10</sup> a<sup>-1</sup> (Min et al. 2000) and an age for FCs of 28.201 ± 0.046 Ma (±2σ, incorporating all sources of error; Kuiper et al. 2008)

e. ±2σ internal error

f. ±2σ full error

g. Ages extrapolated assuming a linear deposition rate between polarity chron boundaries given in Acton et al. (2008a, b) and based on chron ages from GPTS of Gradstein et al. (2004). The last 23 Ma of the GPTS of Gradstein et al. (2004) is orbitally tuned with 40 ka accuracy (see also text)

h. Same as in column g, alternate interpretation

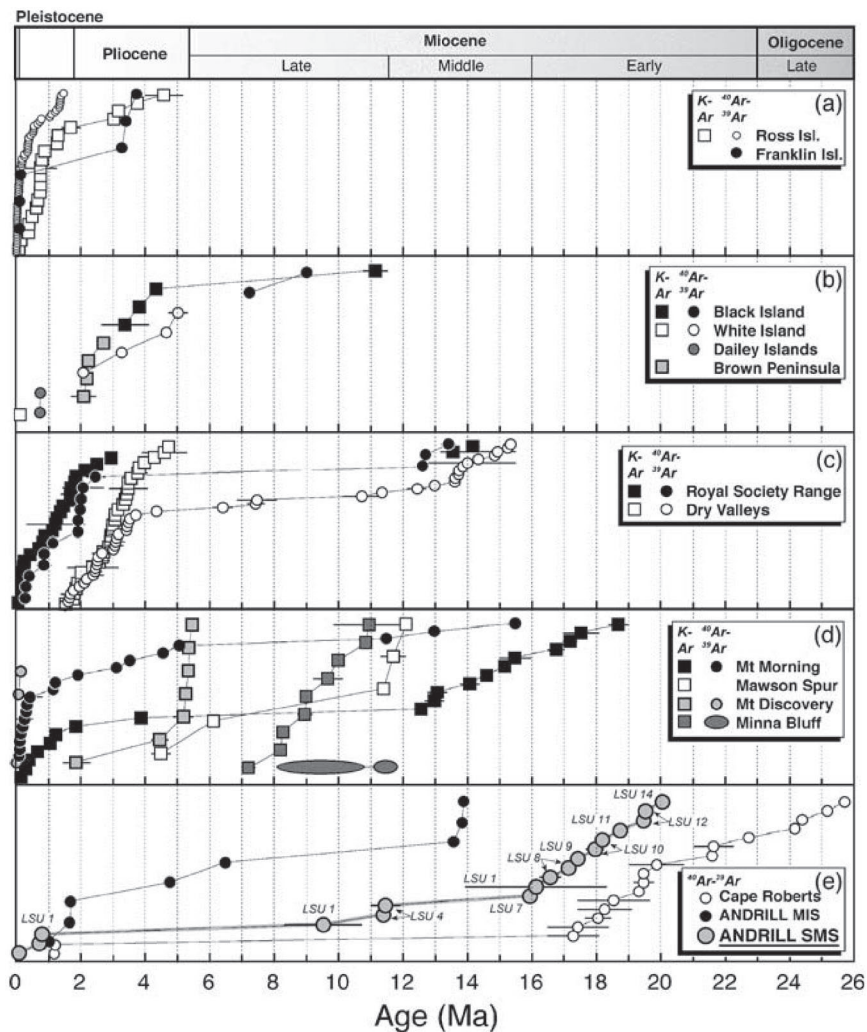


**Figure 6.** Comparison of published K-Ar and  $^{40}\text{Ar}$ - $^{39}\text{Ar}$  ages for volcanic rocks of the Erebus Volcanic Province (a-d) with  $^{40}\text{Ar}$ - $^{39}\text{Ar}$  ages for volcanogenic products from the AND-2A core (this study) and previous drill cores (e). Error bars for all  $^{40}\text{Ar}$ - $^{39}\text{Ar}$  ages are  $2\sigma$  internal uncertainties.  $^{40}\text{Ar}$ - $^{39}\text{Ar}$  ages are relative to an age of 28.03 Ma for the FCs standard (Jourdan and Renne 2007), with the exception of: (1) ages from Rilling et al. (2007) recalculated assuming an age of 28.26 Ma for the FCT-3 standard (Di Vincenzo and Skála 2009); (2) ages from Wilch et al. (1993) recalculated assuming an age of 523.1 Ma for the Mmhb-1 standard (Renne et al. 1998); (3) ages from Tauxe et al. 2004 recalculated assuming an age of 28.34 Ma for the TCs standard (Renne et al. 1998). Error bars for K-Ar ages refer to the uncertainties originally reported by the authors.  $^{40}\text{Ar}$ - $^{39}\text{Ar}$  ages are from: Wilch et al. (1993); Marchant et al (1996); McIntosh (1998, 2000); Esser et al (2004); Harpel et al. (2004); Tauxe et al 2004; Cooper et al. (2007); Lewis et al. (2007); Rilling et al. (2007); Wilson et al. (2007); Kelly et al. (2008); Del Carlo et al. (2009); Lawrence et al. (2009); Martin et al. (2009); Paulsen and Wilson (2009). K-Ar ages are from Kyle and Muncy (1989) and those listed in Kyle 1990. Ellipses in d show age intervals based on new  $^{40}\text{Ar}$ - $^{39}\text{Ar}$  analyses recently reported for Minna Bluff (Fargo et al. 2008). See Figure 1 for localities. LSU = lithostratigraphic unit.

volcanic deposits on land ranging from ~19 Ma (oldest K-Ar whole rock age from Mount Erebus) to Recent (Mount Erebus). Furthermore, previous drill cores in the Cape Roberts area (CRP-1 and CRP-2A; Barrett 2007 – Figure 1) extend the volcanic activity in the area back to the Late Oligocene (McIntosh 1998, 2000).

Sample 8.88–9.02 from the Lithostratigraphic Unit 1, with its young eruption age of <80 ka (Table 2), phonolite composition and large alkali feldspar phenocrysts rich in melt inclusions, compares remarkably with volcanic products from Mount Erebus (Kyle et al. 1992; Esser et al. 2004; Kelly et al. 2008). However, as discussed

in Del Carlo et al. (2009), this sample most probably represents a glacial dropstone, and it is not truly part of the Lithostratigraphic Unit 1. Clasts 10.22–10.44 and 12.23–12.41 have basaltic compositions and compositionally and temporally match the products of the volcanic activity documented for Dailey Islands (~15 km to the south-southwest of the SMS drill site, Figure 1). These samples are interpreted to be sourced from local vents associated with a submerged extension of the Dailey Islands volcanic field (Del Carlo et al. 2009). The basaltic samples 18.03–18.25 and 18.69–18.73, both display ages (~16 and ~10 Ma, respectively) significantly older than those rea-

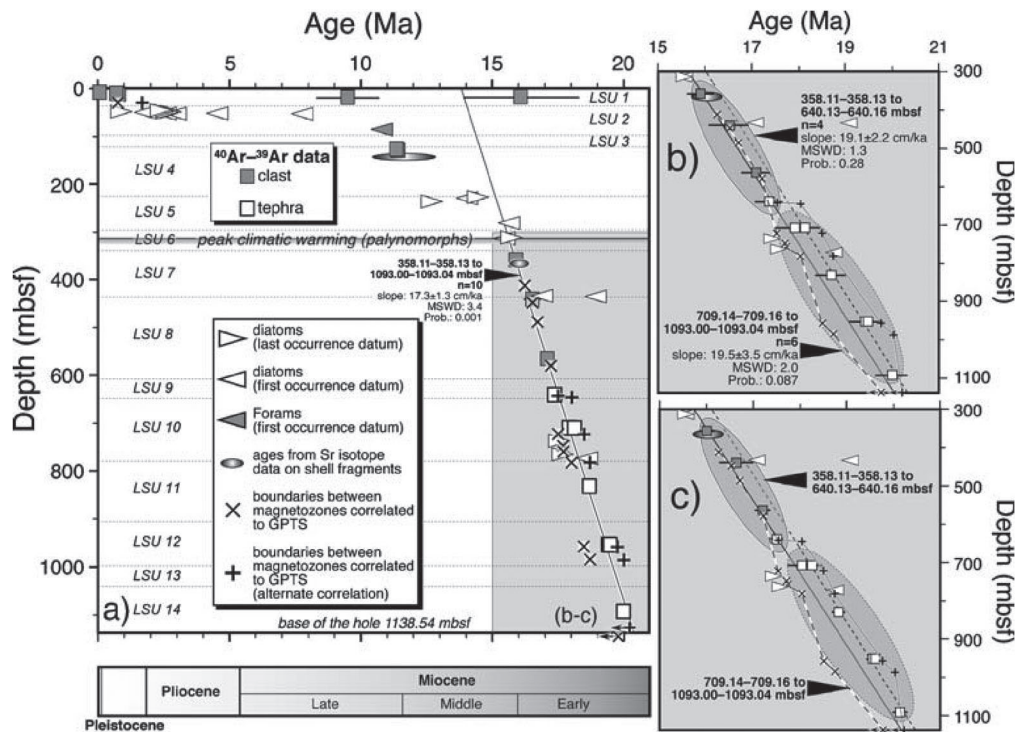


**Figure 7.** Depth vs. age diagram of volcanic samples from the AND-2A core investigated in this study. Ages are listed in Table 2. **a, b** ages calculated using the IUGS recommended constants (Steiger and Jäger 1977) and an age of 28.03 Ma for the fluence monitor FCs (Jourdan and Renne 2007). Error bars are  $2\sigma$  full uncertainties. Results of least squares fit through samples 358.11–358.13 to 1,093.00–1,093.04 (**a**) and through samples 358.11–358.13 to 640.13–640.16 and samples 709.14–709.16 to 1,093.00–1,093.04 (**b**) using  $2\sigma$  internal errors are also shown. **c** Ages calculated using a  $^{40}\text{K}$  total decay constants of  $(5.463 \pm 0.214) \cdot 10^{-10} \text{ a}^{-1}$  (Min et al. 2000) and an age for FCs of  $28.201 \pm 0.046 \text{ Ma}$  ( $\pm 2\sigma$ , incorporating all sources of error; Kuiper et al. 2008). Error bars are  $2\sigma$  full uncertainties. Ages from paleomagnetic and paleontological data, and ages based on Sr isotope compositions of shell fragments are from Acton et al. (2008a, b) and Taviani et al. (2008). Peak of climatic warming based on palynological signal in the AND-2A core from Warny et al. (2009). GPTS Geological Polarity Time Scale (Gradstein et al. 2004). LSU = lithostratigraphic unit.

sonably assumed for the depth of sampling (Figure 7). These samples, therefore, were long reworked before final deposition, and the older basalt may represent materials transported by the Koettlitz Glacier to the McMurdo Ice Shelf from deposits on the north side of Mount Morning (e.g., Kyle and Muncy 1989; Kyle 1990b). The composition (Del Carlo et al. 2009) and age of the younger sample (18.69–18.73) correlate well with volcanic deposits found along the eastern end of Minna Bluff (i.e., Minna Hook; Figure 1).

Samples 127.50–127.52 and 129.96–129.97 from the Lithostratigraphic Unit 4 are clasts of different composition, felsic vs. basaltic, that yielded indistinguishable ages falling at the Middle/Late Miocene boundary ( $\sim 11.4 \text{ Ma}$ , Table 2). Possible sources for these samples (Figure 6) are volcanic rocks from Mason Spur (Kyle 1990b) and/or Minna Bluff (Kyle 1990b; Fargo et al. 2008). Indeed, the age of volcanic products from both Minna Hook ( $11.86 \pm 0.06$  to  $11.20 \pm 0.10 \text{ Ma}$ ; Fargo et al. 2008) and Mason Spur ( $11.4 \pm 0.2$ ,  $11.7 \pm 0.4$  and  $12.1 \pm 0.2 \text{ Ma}$ , Wright-Grassham 1987;  $11.4 \pm 0.1 \text{ Ma}$ , Martin et al. 2009) match those found for the investigated samples from the Lithostratigraphic Unit 4. However, the com-

position of volcanic rocks from Minna Bluff is overall more alkaline, plotting close to the trachyte–phonolite join, thus making provenance from Mason Spur more likely. If this is the case, ice flow or ocean currents were able to transport volcanic clasts from Mason Spur to the north without obstruction.

Samples from Lithostratigraphic Unit 7 to 14 (358.11–358.13 to 1,093.00–1,093.04) yielded ages in the range of  $15.91 \pm 0.14$  to  $20.01 \pm 0.12 \text{ Ma}$  (Table 2 and Figure 6). Volcanic deposits on land with ages falling within this time interval are only known for the older deposits of Mount Morning, cropping out on its northern slopes above the Koettlitz Glacier side (Gandalf Ridge; Figure 1). K–Ar ages for rock samples from this area, varying in composition from trachyandesite to comenditic trachyte, are in the range of  $15.5 \pm 0.5$  to  $18.73 \pm 0.32 \text{ Ma}$  (Kyle and Muncy 1989). Comparable or even older ages (up to  $25.69 \pm 0.16 \text{ Ma}$ , Figure 6) are known for groundmasses and alkali feldspar separates from ash layers or lava clasts sampled in the Cape Roberts drill cores (McIntosh 1998, 2000). The AND-2A core, therefore, contains the oldest known volcanogenic products of the Erebus Volcanic Province after those recovered from the

Cape Roberts drill cores. On the basis of the data available so far, lava clasts in the AND-2A core sampled below ~350 m bsf and with ages older than ~15.5 Ma, were most likely derived from deposits on Mount Morning. Furthermore, explosive activity that produced the tephra found in AND-2A and Cape Roberts cores, as well as older (>13 Ma) tephra deposits in the Dry Valleys (Marchant et al. 1996; Lewis et al. 2007) were likely sourced from vents that have been eroded or are buried beneath the younger deposits on Mount Morning. A “proto-Mount Morning” source for most if not all Early Miocene to Late Oligocene volcanism in the Erebus Volcanic Province is consistent with the progressive shift in volcanic activity away from the continent (i.e., the Mount Morning area) beginning around 13 Ma. Results from the present study reinforce the notion that the Mount Morning is a long-lived eruptive center, a feature which has been explained by its position on the active West Antarctic Rift System within the stationary Antarctic plate (Martin et al. 2009).

***Implications for the age model of the AND-2A core and for sediment deposition in the Victoria Land Basin since the Early Miocene***

Other age constraints (magnetostratigraphic and paleontological temporal constraints and ages based on Sr isotope compositions of shell fragments), useful for the age model of the AND-2A core, are discussed in Acton et al. (2008a, b) and Taviani et al. (2008), and are compared to the whole set of  $^{40}\text{Ar}$ - $^{39}\text{Ar}$  data in Figure 7. Note that the geological polarity time scale (GPTS) of Gradstein et al. (2004) for the last 23 Ma (Neogene), which was used in Acton et al. (2008a, b), is based on astronomical cycles in sediments (orbitally tuned with 40 ka accuracy) and is, therefore, independent of radioisotopic dating.  $^{40}\text{Ar}$ - $^{39}\text{Ar}$  ages quoted in this section and followed by subscript (K) refer to ages calculated using constants from Kuiper et al. (2008) and are considered to be more reliable than those calculated using  $^{40}\text{K}$  decay constants in current use by geochronologists (see above).

In the 0–44.06-m bsf interval, encompassing the Lithostratigraphic Unit 1 and the first 7 m of Lithostratigraphic Unit 2, no age diagnostic taxa were observed (Taviani et al. 2008). In addition, due to the coarse grain size of lithologies encountered in the upper part of the core, interpretation of paleomagnetic data from the Lithostratigraphic Unit 1 to 4 (0–224.82 m bsf) was problematic (Acton et al. 2008a, b), with the only exception being the possible Brunhes/Matuyama reversal (0.781 Ma) or, and alternatively, any other reverse-to-normal transition younger than 2.5 Ma, encountered at 31.10 m bsf. This implies that the only direct temporal constraints for Lithostratigraphic Unit 1 come from  $^{40}\text{Ar}$ - $^{39}\text{Ar}$  data on volcanic clasts. As discussed above,

petrographic, and geochronological data allow the correlation of clast 8.88–9.02 to the pre-caldera summit flows of Mount Erebus. This would imply a sediment supply to the basin from the north and an unlikely very fast subsidence rate (>~500 cm/ka). However, most probably this sample is not truly part of the Lithostratigraphic Unit 1, being its position in the core simply coincidental and a product of recent glacial drift (Del Carlo et al. 2009). Among the remaining four mafic clasts, samples 18.03–18.25 and 18.69–18.73 gave unrealistically old ages for the depth of sampling, consistent with a long transport and reworking before final deposition, whereas samples 10.22–10.44 and 12.23–12.41 provide more realistic ages for the depth of sampling ( $0.696 \pm 0.040_{(K)}$  and  $0.798 \pm 0.065_{(K)}$  Ma, respectively; Table 2). These ages, although strictly constraining maximum ages of deposition, suggest that the first 16 m of the core are younger than 1 Ma. More significantly, in light of the 380 m water depth at the site of drilling and of evidence for shallow water sedimentation for the whole Lithostratigraphic Unit 1 (down to ~37 m bsf; Del Carlo et al. 2009), these data suggest that the mean rate of sedimentation ( $\leq 1.5 \pm 3.2$  and  $1.5 \pm 4.0$  cm/ka,  $\leq 2.0 \pm 1.4$  cm/ka when both samples are used together) did not keep pace with that of basin subsidence (mean rate  $\geq 56.1 \pm 3.2$  and  $49.2 \pm 4.0$  cm/ka), the latter being ~40 times faster. Further, the alignment of Ar data in a depth vs. age diagram suggests that the reverse-to-normal transition encountered at 31.10 m bsf most probably corresponds to the boundary between Chron C2n and C2r.1r (1.945 Ma).

No age data have been obtained for Lithostratigraphic Units 2 and 3 (37.07 to 122.86 m bsf) but two clasts from the Lithostratigraphic Unit 4 (127.50–127.52 and 129.96–127.97) yielded concordant ages of  $11.432 \pm 0.091_{(K)}$  and  $11.50 \pm 0.48_{(K)}$  Ma that overlap within internal errors (Table 2). These ages match a Sr isotope age of ~11.7 Ma from the 144.03–144.06 m bsf interval (Acton et al. 2008a) and are in line with the maximum age of deposition of 11.04 Ma for the 83.76–83.80-m bsf interval, inferred from foraminifera data (Taviani et al. 2008). Our geochronological data along with the independent age constraints suggest that sediments in the upper part of Lithostratigraphic Unit 4 were deposited at the Late/Middle Miocene boundary.

From the Lithostratigraphic Unit 6/7 boundary (339.92 m bsf) to the base of hole, samples investigated by the  $^{40}\text{Ar}$ - $^{39}\text{Ar}$  method are more uniformly distributed (Figure 7). This, along with paleomagnetic data, whose quality below the Lithostratigraphic Unit 7/8 boundary improves significantly so as to provide a continuous polarity stratigraphy for the ~340–1,139-m bsf interval (Acton et al. 2008a, b), allows the reconstruction of a robust age model and, more in general, a thorough comparison between temporal constraints based on radioisotopic and paleomagnetic data. Ana-

lyzed samples from the ~358–1,093-m bsf interval consist of three clasts and seven samples from primary to moderately reworked tephra layers, the former covering the uppermost part of the core interval (from ~358 to ~565 m bsf) and the latter the lowermost ~450 m (from ~640 to the base of the hole). In a depth vs. age plot (Figure 7), data from the three clasts are aligned along the same trend with a negative slope defined by the seven tephra layers, suggesting that the three clasts yield Ar ages which closely approach the time of deposition and that the whole sample set provide a nearly continuous depositional record. A least-squares fit for the whole set of data using internal errors (Figure 7a) yields a MSWD of 3.4 and a slope of  $17.3 \pm 1.3$  cm/ka. The MSWD value, although surprisingly low for a core ~735 m in length, and corresponding to a time interval of ~4.1 Ma, given the degrees of freedom of the whole dataset (i.e., 8, probability of fit 0.001), indicates that the use of a single regression line is not entirely justified (i.e., the scatter exceeds the purely analytical one). Close inspection of Figure 7 indeed reveals that the distribution of data points is best accounted for by two regression lines, one through the upper four samples (358.11–358.13, 440.83–440.86, 564.92–564.93, and 640.13–640.16) and the second through the remaining lower six samples (709.14–709.16, 709.17–709.19, 831.66–831.68, 953.28–953.31, 953.54–953.56, and 1,093.00–1,093.04). The regression lines are both statistically acceptable, with a probability of fit  $\gg 0.05$  (Figure 7b and c), and yield mean sedimentation rates of  $19.1 \pm 2.2$  and  $19.5 \pm 3.5$  cm/ka, overlapping within errors. These arguments indicate that Ar data from the ~358–1,093-m bsf interval records a relatively fast and constant mean sedimentation rate of ~19 cm/ka, with a possible break in between ~640 and ~709 m bsf (~17.4 and ~18.0 Ma, respectively), characterized instead by a mean sedimentation rate as low as  $9.9 \pm 2.6$  cm/ka. Coincidentally, an abrupt erosional contact was identified at 648.74 m bsf and was taken as the boundary between Lithostratigraphic Unit 9 and the underlying Lithostratigraphic Unit 10 (Fielding et al. 2008b). Furthermore, based on paleontological data (Figure 7), such a fast mean sedimentation rate should have persisted up to ~310–312 m bsf, where diatom data indicate that sedimentation occurred within 15.50–15.70 Ma (Taviani et al. 2008). In light of the large time interval encompassing the two identified intervals (i.e., ~1.5 and ~1.9 Ma) and of available sedimentologic data (Fielding et al. 2008b), it is very unlikely, however, that sedimentation was truly constant even within the 358–640- and 709–1096-m bsf intervals. Rather, results should be interpreted to indicate that departure (possible oscillations) from a linear sedimentation rate, not only true variations in deposition rate but also hiatuses, should have been no longer than  $2\sigma$  internal errors (Table 2), that is less than a few hundreds of ka.

This simple observation is intriguing since oscillations with periods of  $\leq 400$  ka encompass those of orbital perturbations (Milankovitch cycles).

From a broader perspective, it is important to note that recent investigation on the AND-2A sediment core (Warny et al. 2009) has revealed within the 310–312-m bsf interval a palynological assemblage documenting a relatively short period of time during which Antarctica became suddenly much warmer. This ice-proximal record of past Antarctic climate, suggesting that warming peaked at ~15.7 Ma, matches the Middle Miocene Climate Optimum, a period (14–16 Ma) during which the Earth was warmer than today and which was followed by a gradual cooling toward a more stable ice-house period (Zachos et al. 2001; Shevenell et al. 2004). While it is beyond the scope of this work to draw general conclusions about the paleoclimatic implications of the AND-2A core, a few prominent features of the stratigraphic record need to be pointed out (Figure 7): (1) the coincidence of the nearly continuous Early to Middle Miocene record with a period during which glaciers in the area are hypothesized to have been wet-based and possibly more erosive (e.g., Sudgen and Denton 2004); (2) the concomitance of the warmer period (Warny et al. 2009) with the upper termination of the nearly continuous Early to Middle Miocene section; (3) the coincidence of the change in style and rate of deposition from the Middle Miocene onward with the hypothesized shift from wet- to cold-based glaciers (~14 Ma—Sudgen and Denton 2004; Lewis et al. 2007) and with a climate degradation on a global scale (e.g., Shevenell et al. 2004); (4) the consistency of the condensed and discontinuous Middle Miocene to Recent record with an environment close to the margin of a dynamic ice sheet (Naish et al. 2009; McKay et al. 2009). The above arguments suggest that future research on the AND-2A sediment core have a strong potential to shed light on the apparent inconsistency between a scenario in which the East Antarctic Ice Sheet became stable and cold starting from about 14 Ma (Sudgen and Denton 2004; Lewis et al. 2007), and another in which the Antarctic Ice Sheets instead underwent important fluctuations over the past 13 Ma, with repetitive oscillations of ice-sheet extent (McKay et al. 2009).

On the basis of preliminary  $^{40}\text{Ar}$ - $^{39}\text{Ar}$  ages and available paleontological data, Acton et al. (2008a, b) correlated paleomagnetic data from the 328.52–581.34-m bsf interval with Chron C5Cn.1n (15.974–16.268 Ma) to Chron C5Cr (16.721–17.235 Ma). Polarity chron boundaries from the abovementioned interval yield ages that match within error those obtained from  $^{40}\text{Ar}$ - $^{39}\text{Ar}$  data, irrespective of the constants used in the calculation of Ar ages (Figure 7 and Table 2). Below 581.34 m bsf, however, interpretation of paleomagnetic data is more uncertain (Acton et al. 2008a, b), as the identified magnetozone may be either correlated with



Chron C5Dn (17.235–17.533 Ma) to Chron C6n (18.748–19.772 Ma) or with Chron C5Dn to Chron C6An.1n (20.040–20.213 Ma), with polarity chron boundaries differing in age by as much as ~1.3 Ma (Figure 7 and Table 2). Correlation of paleomagnetic data with Chrons C5Dn to C6n, however, would imply that volcanic materials from 709.14 m bsf down hole were reworked long before final deposition. Indeed, assuming a linear sedimentation rate between tie points, paleomagnetic data would yield ages that are significantly younger than those from radioisotopic data, even when full errors are taken into account (Table 2): ages extrapolated from paleomagnetic data are  $0.43 \pm 0.40$  to  $0.98 \pm 0.34$  Ma and  $0.54 \pm 0.31$  to  $1.10 \pm 0.17$  Ma younger than  $^{40}\text{Ar}$ – $^{39}\text{Ar}$  ages calculated using constants of Steiger and Jäger (1977) and those proposed by Kuiper et al. (2008), respectively. In light of petrographic data, of the alignment of  $^{40}\text{Ar}$ – $^{39}\text{Ar}$  age data in a depth vs. age diagram (Figure 7), as well as of paleontologic and paleomagnetic data both independently suggesting a relatively fast mean sedimentation rate below ~300 m bsf down hole, such a long reworking time for the studied samples seems to be a very unlikely possibility. Correlation of paleomagnetic data below 581.34-m bsf with Chron C5Dn to Chron C6An.1n would instead yield a better fit with radioisotopic ages. With the exception of sample 709.17–709.19, yielding an Ar age marginally yet significantly younger than that extrapolated from paleomagnetic data ( $18.04 \pm 0.31_{(K)}$  Ma vs. 18.44 Ma, Table 2), the remaining samples yield Ar ages indistinguishable at the  $2\sigma$  confidence level from those derived from paleomagnetic data (Table 2) extrapolated from bracketing tie points (samples 640.13–640.16, 709.14–709.16, 709.17–709.19, and 1093.00–1093.04) or using the nearest upper (sample 831.66–831.68) or lower tie-points (samples 953.28–953.31 and 953.54–953.56).

### Concluding remarks and general implications

One of the main goals of the ANDRILL SMS Project was to recover an expanded stratigraphic record from the Middle Miocene, in order to fill the gap left by previous drill cores (ANDRILL MIS and Cape Roberts projects). The Middle Miocene (~16.0 to 11.6 Ma; Gradstein et al. 2004) is indeed a key time interval in the construction of modern Antarctic cryosphere. This period hosts the Middle Miocene climate transition (14.2–13.8 Ma), which followed the Middle Miocene Climate Optimum and represents one of the key steps in the Cenozoic climate cooling (Zachos et al. 2001, 2008; Shevenell et al. 2004).

$^{40}\text{Ar}$ – $^{39}\text{Ar}$  laser analyses on volcanic rocks of the AND-2A core from the present study, in conjunction with petrographic data, reveal that the SMS project recovered as much as  $\leq 230$  m of Middle Miocene and as

much as  $>780$  m of Early Miocene. Results indicate that future chronostratigraphic work should concentrate in the ~128–358-m bsf interval of the core in order to improve chronological control of the AND-2A core corresponding to Middle Miocene. More significantly, data from the present study reveal that the ~358–1,093-m bsf interval of the core, corresponding to the Early Miocene (from ~16.0 to ~20.1 Ma), yields a nearly continuous stratigraphic record, characterized by a relatively fast and a nearly constant mean sedimentation rate of ~19 cm/ka, with a possible break in between ~640 and ~709 m bsf. In light of available independent chronological constraints for the AND-2A core, such a style of sedimentation should have persisted up to ~310 m bsf, corresponding to the beginning of Middle Miocene. It is important to note, however, that the available stratigraphy of the area (e.g., Fielding et al. 2008a) along with sedimentologic data from the AND-2A core (Fielding et al. 2008b), suggest that sedimentation was not truly constant in that period.  $^{40}\text{Ar}$ – $^{39}\text{Ar}$  age data therefore should be interpreted to indicate that departure (possible oscillations) from a linear sedimentation rate did not exceed a few hundreds of ka.

Preservation of a relatively thick and nearly continuous Early to Middle Miocene sedimentary sequence underlying a condensed and discontinuous Middle Miocene to Recent section is in line with and reinforces the model proposed by Fielding et al. (2008a) for the evolution of the Cenozoic Victoria Land Basin of the West Antarctic Rift System. According to Fielding et al. (2008a), the Victoria Land Basin during Early to Middle Miocene (23 to 13 Ma) underwent a phase of passive thermal subsidence, that occurred in between Early Rift and Main Rift phases (within 29–23 Ma), producing the Victoria Land Basin, and a Renewed Rift phase (13 Ma to Recent) that produced the Terror Rift. Indeed, an Early Miocene phase of passive subsidence can explain the nearly continuous stratigraphic record (Fielding et al. 2008b) and the constant and relatively fast mean sedimentation rate calculated here. A renewed rift phase (Middle Miocene to Recent) that produced the Terror Rift with erosion of its western boundary and a shift in the locus of sedimentation to the east, instead accounts for a condensed and discontinuous stratigraphic record in the upper portion of the core ( $<225$  m bsf,  $<14$  Ma).

Comparison with available geochronological data from volcanic deposits on land of the Erebus Volcanic Province suggests that investigated volcanogenic products were supplied from the south, possibly with source deposits becoming closer to the drill site at upper core levels. As for the nearly continuous Early Miocene stratigraphic record, Ar data suggest derivation from volcanic deposits of the “proto-Mount Morning,” that is more or less from a “point-source.” This is consistent with the observation that during the Early Miocene, before the construction of Minna Bluff ( $>13$  Ma),

there was no obstruction to ice flow or ocean currents. Furthermore, this would imply that the front of the ice shelf (when and if present at that time) would have had a pinning line at "proto-Mount Morning" or further south. Ice flow or ocean currents were able to transport volcanic clasts from Mason Spur to the north without obstruction from Minna Bluff up until at least the Late Miocene (~11.5 Ma).

**Acknowledgments** – The journal reviews of S. Hemming and W. LeMasurier and the editorial handling by M. A. Clyne for *Bulletin of Volcanology* are gratefully acknowledged. G.D.V. is indebted to W. McIntosh, who kindly provided the fluence monitor Fish Canyon sanidine. The ANDRILL Program is a multinational collaboration between the Antarctic programs of Germany, Italy, New Zealand, and USA. Antarctica New Zealand is the project operator and developed the drilling system in collaboration with Alex Pyne at Victoria University of Wellington and Webster Drilling and Exploration Ltd. Antarctica New Zealand supported the drilling team at Scott Base; Raytheon Polar Services Corporation supported the science team at McMurdo Station and the Crary Science and Engineering Centre. The ANDRILL Science Management Office at the University of Nebraska-Lincoln provided science planning and operational support. Scientific studies are jointly supported by the US National Science Foundation (NSF), NZ Foundation for Research, Science and Technology (FRST), the Italian Antarctic Research Program (PNRA), the German Research Foundation (DFG) and the Alfred Wegener Institute (AWI) for Polar and Marine Research. The Ar-Ar laserprobe facility was funded by the PNRA and the CO<sub>2</sub> laser system by the Consiglio Nazionale delle Ricerche.

## References

- Acton G, Crampton J, Di Vincenzo G, Fielding CR, Florindo F, Hannah M, Harwood D, Ishman S, Johnson K, Covane L, Levy R, Lum B, Marcato MC, Mukasa S, Ohneiser C, Olney M, Riesselman C, Sagnotti L, Stefano C, Strada E, Tavianini M, Tuzzi E, Verosub KL, Wilson GS, Zattin M (2008a) Preliminary integrated chronostratigraphy of the AND-2A core, ANDRILL Southern McMurdo Sound Project. In: Harwood DM, Florindo F, Talarico F, Levy RH (eds) Studies from the ANDRILL, Southern McMurdo Sound Project, Antarctica. *Terra Antart* 15 (in press)
- Acton G, Florindo F, Jovane L, Lum B, Ohneiser C, Sagnotti L, Strada E, Verosub KL, Wilson GS (2008b) Palaeomagnetism of the AND-2A Core, ANDRILL Southern McMurdo Sound Project, Antarctica. In: Harwood DM, Florindo F, Talarico F, Levy RH (eds) Studies from the ANDRILL, Southern McMurdo Sound Project, Antarctica. *Terra Antart* 15 (in press)
- Bachmann O, Oberli F, Dungan MA, Meier M, Mundil R, Fischer H (2007)  $^{40}\text{Ar}/^{39}\text{Ar}$  and U-Pb dating of the Fish Canyon magmatic system, San Juan Volcanic field, Colorado: evidence for an extended crystallization history. *Chem Geol* 236:134–166
- Barrett PJ (1987) Oligocene sequence cored at CIROS-1, western McMurdo Sound. *New Zealand Antarctic Record* 7:1–17
- Barrett PJ (2007) Cenozoic climate and sea level history from glacial marine strata off the Victoria Land coast, Cape Roberts Project, Antarctica. In: Hambrey MJ, Christoffersen P, Glasser NF, Hubbard B (eds) *Glacial processes and products*. Blackwell, New York, pp 259–287
- Cooper AK, Davey FJ, Behrendt JC (1987) Seismic stratigraphy and structure of the Victoria Land Basin, western Ross Sea, Antarctica. In: Cooper AK, Davey FJ (eds) *The Antarctic Continental margin: geology and geophysics of the Western Ross Sea*, 5b. Circum-Pacific Council for Energy and Natural Resources Earth Science, Reston, pp 27–76
- Cooper AF, Lotte JA, Coulter RF, Nelson Eby G, McIntosh WC (2007) Geology, geochronology and geochemistry of a basaltic volcano, White Island, Ross Sea, Antarctica. *J Volcanol Geoth Res* 165:189–216. doi: 10.1016/j.jvolgeores.2007.06.003
- Del Carlo P, Panter KS, Bassett K, Bracciali L, Di Vincenzo G, Rocchi S (2009) Evidence for local volcanic sources in the upper lithostratigraphic unit of ANDRILL AND-2A core (Southern McMurdo Sound, Antarctica) and implications for paleoenvironment and subsidence in the western Victoria Land basin. *Global Planet Change* 69:142–161. doi: 10.1016/j.gloplacha.2009.09.002
- Di Vincenzo G, Skála R (2009)  $^{40}\text{Ar}$ - $^{39}\text{Ar}$  laser dating of tektites from the Cheb Basin (Czech republic): Evidence for coevality with moldavites and influence of the dating standard on the age of the Ries impact. *Geochim Cosmochim Acta* 73:493–513. doi: 10.1016/j.gca.2008.10.002
- Dibble RR, Kyle PR, Rowe CA (2008) Video and seismic observations of Strombolian eruptions at Erebus volcano, Antarctica. *J Volcanol Geoth Res* 177:619–634. doi: 10.1016/j.jvolgeores.2008.07.020
- Esser RP, McIntosh WC, Heizler MT, Kyle PR (1997) Excess argon in melt inclusions in zero-age anorthoclase feldspar from Mt. Erebus, Antarctica as revealed by the  $^{40}\text{Ar}/^{39}\text{Ar}$  method. *Geochim Cosmochim Acta* 61:3789–3801
- Esser RP, Kyle PR, McIntosh WC (2004)  $^{40}\text{Ar}/^{39}\text{Ar}$  dating of the eruptive history of Mount Erebus, Antarctica: volcano evolution. *Bull Volcanol* 66:671–686. doi: 10.1007/s00445-004-0354-x
- Fargo AJ, McIntosh WC, Dunbar NW, Wilch TI (2008)  $^{40}\text{Ar}$ - $^{39}\text{Ar}$  geochronology of Minna Bluff, Antarctica: timing of Mid-Miocene glacial erosional events within the Ross Embayment. *Eos Trans. AGU*, 89(53), Fall Meet Suppl, Abstract V13C-2127
- Fielding CR, Whittaker J, Henrys SA, Wilson TJ, Naish TR (2008a) Seismic facies and stratigraphy of the Cenozoic succession in McMurdo Sound, Antarctica: implications for tectonic, climate and glacial history. *Palaeogeogr Palaeoclimatol* 260:8–29. doi: 10.1016/j.palaeo.2007.08.016
- Fielding CR, Atkins CB, Bassett KN, Browne GH, Dunbar GB, Field BD, Frank TD, Panter KS, Pekar SF, Krissek LA, Passchier S (2008b) Sedimentology and stratigraphy of the AND-2A core, ANDRILL Southern McMurdo Sound, Project, Antarctica. In: Harwood DM, Florindo F, Talarico F, Levy RH (eds) Studies from the ANDRILL, Southern McMurdo Sound Project, Antarctica. *Terra Antart* 15 (in press)
- Florindo F, Harwood D, Levy R (2008) SMS Project Science Team (2008) ANDRILL's success during the 4th International Polar Year. *Scientific Drilling* 6:29–31

- Flower BP, Kennett JP (1994) The middle Miocene climatic transition: East Antarctic ice sheet development, deep ocean circulation and global carbon cycling. *Palaeogeogr Palaeoclimatol* 108:537–555
- Gamble JA, Barrett PJ, Adams CJ (1986) Basaltic clasts from Unit 8. *Bulletin of New Zealand DSIR* 237:145–152
- Gradstein FM, Ogg JG, Smith AG (2004) *A geologic time scale 2004*. Cambridge University Press, Cambridge, p 610
- Harwood DM, Florindo F, Talarico F, Levy RH, Acton G, Fielding C, Panter K, Paulsen T, Taviani M (2008) Synthesis of the Initial Scientific Results of the ANDRILL Southern McMurdo Sound Project, Victoria Land Basin, Antarctica. In: Harwood DM, Florindo F, Talarico F, Levy RH (eds) *Studies from the ANDRILL, Southern McMurdo Sound Project, Antarctica*. *Terra Antart* 15 (in press)
- Harpel CJ, Kyle PR, Esser RP, McIntosh WC, Caldwell DA (2004)  $^{40}\text{Ar}/^{39}\text{Ar}$  dating of the eruptive history of Mount Erebus, Antarctica: summit flows, tephra, and caldera collapse. *Bull Volcanol* 66:687–702. doi: 10.1007/s00445-004-0349-7
- Holbourn A, Kuhnt W, Schulz M, Flores J-A, Andersen N (2007) Orbitally-paced climate evolution during the Middle Miocene “Monterey” carbon-isotope excursion. *Earth Planet Sci Lett* 261:534–550. doi: 10.1016/j.epsl.2007.07.026
- Johnston L, Wilson GS, Gorman AR, Henrys SA, Horgan H, Clark R, Naish TR (2008) Cenozoic basin evolution beneath the southern McMurdo Ice Shelf, Antarctica. *Global Planet Change* 62:61–76. doi: 10.1016/j.gloplacha.2007.11.004
- Jourdan F, Renne PR (2007) Age calibration of the Fish Canyon sanidine  $^{40}\text{Ar}/^{39}\text{Ar}$  dating standard using primary K–Ar standard. *Geochim Cosmochim Acta* 71:387–402. doi: 10.1016/j.gca.2006.09.002
- Kelly PJ, Kyle PR, Dunbar NW, Sims KWW (2008) Geochemistry and mineralogy of the phonolite lava lake, Erebus volcano, Antarctica: 1972–2004 and comparison with older lavas. *J Volcanol Geoth Res* 177:589–605. doi: 10.1016/j.jvolgeores.2007.11.025
- Koppers AAP, Staudigel H, Wijbrans JR (2000) Dating crystalline groundmass separates of altered Cretaceous seamount basalts by the  $^{40}\text{Ar}/^{39}\text{Ar}$  incremental heating technique. *Chem Geol* 166:139–158
- Krumrei TV, Villa IM, Marks MAW, Markl G (2006) A  $^{40}\text{Ar}/^{39}\text{Ar}$  and U/Pb isotopic study of the Ilímaussaq complex, South Greenland: implications for the  $^{40}\text{K}$  decay constant and for the duration of magmatic activity in a peralkaline complex. *Chem Geol* 227:258–273. doi: 10.1016/j.chemgeo.2005.10.004
- Kuiper KF, Deino A, Hilgen FJ, Krijgsman W, Renne PR, Wijbrans JR (2008) Synchronizing rock clocks of Earth history. *Science* 320:500–504. doi: 10.1126/science.1154339
- Kyle PR (1990a) McMurdo Volcanic Group - Introduction. In: LeMasurier WE, Thomson JW (eds) *Volcanoes of the Antarctic plate and Southern Oceans*. Antarctic research series 48. American Geophysical Union, Washington, pp 19–25
- Kyle PR (1990b) Erebus Volcanic Province - Summary. In: LeMasurier WE, Thomson JW (eds) *Volcanoes of the Antarctic Plate and Southern Oceans*. Antarctic research series 48. American Geophysical Union, Washington, pp 81–135
- Kyle PR, Cole JW (1974) Structural control of volcanism in the McMurdo Volcanic Group, Antarctica. *Bull Volcanol* 38:16–25
- Kyle PR, Muncy HL (1989) Geology and geochronology of McMurdo Volcanic Group rocks in the vicinity of Lake Morning, McMurdo Sound, Antarctica. *Antarct Sci* 1:345–350
- Kyle PR, Moore JA, Thirlwall MF (1992) Petrologic evolution of anorthoclase phonolite lavas at Mount Erebus, Ross Island, Antarctica. *J Petrol* 33:849–875
- Lawrence KP, Tauxe L, Staudigel H, Constable CG, Koppers A, McIntosh W, Johnson CL (2009) Paleomagnetic field properties at high southern latitude. *Geochem Geophys Geosyst* 10:Q01005. doi: 10.1029/2008GC002072
- Lewis AR, Marchant DR, Ahworth AC, Hemming SR, Machlus ML (2007) Major middle Miocene global climate change: evidence from East Antarctica and the Transantarctic Mountains. *Geol Soc Am Bull* 119:1449–1461. doi: 10.1130B26134.1
- Marchant DR, Denton GH, Swisher CC III, Potter N Jr (1996) Late Cenozoic Antarctic paleoclimate reconstructed from volcanic ashes in the Dry Valleys region of southern Victoria Land. *Geol Soc Am Bull* 108:181–194
- Martin AP, Cooper AF, Dunlap WJ (2009) Geochronology of Mount Morning, Antarctica: two-phase evolution of a long-lived trachyte-basanite-phonolite eruptive center. *Bull Volcanol*. doi: 10.1007/s00445-009-0319-1
- McIntosh WC (1998)  $^{40}\text{Ar}/^{39}\text{Ar}$  geochronology of volcanic clasts and pumice in CRP-1 core, Cape Roberts, Antarctica. *Terra Antart* 5:683–690
- McIntosh WC (2000)  $^{40}\text{Ar}/^{39}\text{Ar}$  geochronology of tephra and volcanic clasts in CRP-2A, Victoria Land Basin, Antarctica. *Terra Antart* 7:621–630
- McKay R, Browne G, Carter L, Cowan E, Bunbar G, Krissek L, Naish T, Powell R, Reed J, Talarico F, Wilch T (2009) The stratigraphic signature of the late Cenozoic Antarctica Ice Sheets in the Ross Embayments. *Geol Soc Am Bull* 121:1537–1561. doi: 10.1130/B26540.1
- Min K, Mundil R, Renne PR, Ludwig KR (2000) A test for systematic errors in  $^{40}\text{Ar}/^{39}\text{Ar}$  geochronology through comparison with U–Pb analysis of a 1.1 Ga rhyolite. *Geochim Cosmochim Acta* 64:73–98
- Naish T, Powell R, Levy R, ANDRILL-MIS Science Team (2007) Background to the ANDRILL McMurdo Ice Shelf project (Antarctica) and initial science volume. *Terra Antart* 14:121–130
- Naish T, Powell R, Levy R, Wilson G, Scherer R, Talarico F, Krissek L, Niessen F, Pompilio M, Wilson T, Carter L, DeConto R, Huybers P, McKay R, Pollard D, Ross J, Winter D, Barrett P, Browne G, Cody R, Cowan E, Crampton J, Dunbar G, Dunbar N, Florindo F, Gebhardt C, Graham I, Hannah M, Hansaraj D, Harwood D, Helling D, Henrys S, Hinov L, Kuhn G, Kyle P, Läuffer A, Maffioli P, Magens D, Mandernack K, McIntosh W, Millan C, Morin R, Ohneiser C, Paulsen T, Persico D, Raine I, Reed J, Riesselman C, Sagnotti L, Schmitt D, Sjunneskog C, Strong P, Taviani M, Vogel S, Wilch T, Williams T (2009) Obliquity-paced Pliocene West Antarctic ice sheet oscillations. *Nature* 458:322–328. doi: 10.1038/nature0867
- Panter KS, Talarico F, Bassett K, Del Carlo P, Field B, Frank T, Hoffman S, Kuhn G, Reichelt L, Sandroni S, Taviani M, Bracciali L, Cornamusini G, von Eynatten H, Rocchi R (2008) Petrologic and Geochemical Composition of the AND-2A Core, ANDRILL Southern McMurdo Sound Project, Ant-

- arctica. In: Harwood DM, Florindo F, Talarico F, Levy RH (eds), *Studies from the ANDRILL, Southern McMurdo Sound Project, Antarctica*. Terra Antart 15 (in press)
- Paulsen TS, Wilson TJ (2009) Structure and age of volcanic fissures on Mount Morning: a new constraint on Neogene to contemporary stress in the West Antarctic Rift, southern Victoria Land, Antarctica. *Geol Soc Am Bull* 121:1071-1088. doi: 10.1130/B26333.1
- Pompilio M, Dunbar N, Gebhardt AC, Helling D, Kuhn G, Kyle P, McKay R, Talarico F, Tulaczyk S, Vogel S, Wilch T, ANDRILL-MIS Science Team (2007) Petrology and geochemistry of the AND-1B Core, ANDRILL McMurdo Ice Shelf Project, Antarctica. *Terra Antart* 14:255-288
- Renne PR, Swisher CC, Deino AL, Karner DB, Owens TL, DePaolo DJ (1998) Intercalibrations of standards, absolute ages and uncertainties in  $^{40}\text{Ar}/^{39}\text{Ar}$  dating. *Chem Geol* 145:117-152
- Rilling SE, Mukasa SB, Wilson TJ, Lawver LA (2007)  $^{40}\text{Ar}$ - $^{39}\text{Ar}$  age constraints on volcanism and tectonism in the Terror Rift of the Ross Sea, Antarctica. In: Cooper AK, Raymond CR (eds) *Antarctica: a keystone in a changing world*. Online Proceedings of the 10th ISAES, USGS Open-File Report 2007-1047, Short Research Paper 092, pp 4
- Schoene B, Crowley JL, Condon DJ, Schmitz MD, Bowring SA (2006) Reassessing the uranium decay constants for geochronology using ID-TIMS U-Pb data. *Geochim Cosmochim Acta* 70:426-445. doi: 10.1016/j.gca.2005.09.007
- Shevenell AE, Kennett JP, Lea DW (2004) Middle Miocene Southern Ocean cooling and Antarctic cryosphere expansion. *Science* 305:1766-1770
- Steiger RH, Jäger E (1977) Subcommittee on Geochronology: convention on the use of decay constants in geo- and cosmochemistry. *Earth Planet Sci Lett* 36:359-362
- Sudgen D, Denton G (2004) Cenozoic landscape evolution of the Convoy Range to Mackay Glacier area, Transantarctic Mountains: onshore to offshore synthesis. *Geol Soc Am Bull* 116:840-857. doi: 10.1130/B25356.1
- Tauxe L, Gans P, Mankinen EA (2004) Paleomagnetism and  $^{40}\text{Ar}/^{39}\text{Ar}$  ages from volcanics extruded during the Matuyama and Brunhes Chrons near McMurdo Sound, Antarctica. *Geochem Geophys Geosyst* 5:Q06H12. doi: 10.1029/2003GC000656
- Taviani M, Hannah M, Harwood DM, Ishman SE, Johnson K, Olney M, Riesselman C, Tuzzi E, Askin R, Beu AG, Blair S, Cantarelli V, Ceregato A, Corrado S, Mohr B, Nielsen SHH, Persico D, Petrushak S, Raine JI, Warny S (2008) Palaeontologic Characterization of the AND-2A Core, ANDRILL Southern McMurdo Sound Project, Antarctica. In: Harwood DM, Florindo F, Talarico F, Levy RH (eds) *Studies from the ANDRILL, Southern McMurdo Sound Project, Antarctica*. Terra Antart 15 (in press)
- Van der Wateren FM, Cloetingh SAPL (1999) Feedbacks of lithosphere dynamics and environmental change of the Cenozoic west Antarctic rift system. *Global Planet Change* 23:1-24
- Warny S, Askin RA, Hannah MJ, Mohr BAR, Raine JI, Harwood DM, Florindo F, SMS Science Team (2009) Palynomorphs from a sediment core reveal a sudden remarkably warm Antarctica during the Middle Miocene. *Geology* 37:955-958. doi: 10.1130/G30139A.1
- Wilch TI, Lux DR, Denton GH, McIntosh WC (1993) Minimal Pliocene-Pleistocene uplift of the dry valleys sector of the Transantarctic Mountains: a key parameter in ice-sheet reconstructions. *Geology* 21:841-844
- Wilson G, Levy R, Browne G, Cody R, Dunbar N, Florindo F, Henys S, Graham I, McIntosh W, McKay R, Naush T, Ohneiser C, Powell R, Ross J, Sagnotti L, Schere R, Sjunneskog C, Strong CP, Taviani M, Winter D, ANDRILL-MIS Science Team (2007) Preliminary integrated chronostratigraphy of the AND-1B core, ANDRILL McMurdo Ice Shelf Project, Antarctica. *Terra Antart* 14:297-316
- Wilson TJ (1995) Cenozoic transtension along the Transantarctic Mountains west Antarctic rift boundary, southern Victoria Land, Antarctica. *Tectonics* 14:531-545
- Wilson TJ (1999) Cenozoic structural segmentation of the Transantarctic Mountains rift flank in southern Victoria Land. *Global Planet Change* 23:105-127
- Wilson TJ, Demosthenous CM (2000) SAR-based mapping of glaciated volcanic terrain: the Erebus Volcanic Province, Antarctica. *Can J Remote Sens* 26:142-158
- Wilson TJ, Paulsen T, Wilch TI (2003) Structural control on Neogene-Quaternary volcanism in the Transantarctic Mountains, southern Victoria Land, Antarctica, EGS-AGU-EUG 2003 Joint Assembly, Volume 5: Nice, France, p 14357
- Wright-Grassham AC (1987) Volcanic geology, mineralogy, and petrogenesis of the Discovery Volcanic Subprovince, Southern Victoria Land, Antarctica. PhD thesis, New Mexico Institute of Mining and Technology, Socorro, NM
- Zachos J, Pagani M, Sloan L, Thomas E, Billups K (2001) Trends, rhythms, and aberrations in global climate 65 Ma to Present. *Nature* 292:686-693
- Zachos JC, Dickens GR, Zeebe RE (2008) An early Cenozoic perspective on greenhouse warming and carbon-cycle dynamics. *Nature* 451:279-283. doi: 10.1038/nature06588

## **Supplementary Material**

$^{40}\text{Ar}$ – $^{39}\text{Ar}$  dating of volcanogenic products from the AND-2A core (ANDRILL Southern McMurdo Sound Project, Antarctica): correlations with the Erebus Volcanic Province and implications for the age model of the core

by

G. Di Vincenzo, L. Bracciali, P. Del Carlo, K. Panter, S. Rocchi

### **1. Methods**

### **2. Features of dated rocks**

### **3. Fig. S1**

### **4. Fig. S2**

### **5. Fig. S3**

### **6. Table S1**

## 1. Methods

Sample preparation and  $^{40}\text{Ar}$ – $^{39}\text{Ar}$  data collection were completed at IGG–CNR, Pisa (Italy). Samples selected for  $^{40}\text{Ar}$ – $^{39}\text{Ar}$  dating before processing, that is as received at IGG–CNR laboratory, are shown in Fig. S1. Samples affected by alteration, evident under the optical or electronic microscope, were rejected and not analyzed.

Polished thin sections from each sample were investigated by a light microscope and by scanning electron microscopy (SEM) using a Philips XL30 (using an accelerating voltage of 20 kV, sample current of 10 nA and 0.5  $\mu\text{m}$  beam diameter) equipped with an energy dispersive system (EDS) at the Dipartimento di Scienze della Terra, Pisa.

After crushing and sieving, groundmasses and feldspars (plagioclase or alkali feldspar) were concentrated from different grain sizes (see Tables S1) using standard separation techniques, and further purified by hand-picking under a stereomicroscope. Groundmass separates were leached in an ultrasonic bath (heated to  $\sim 50^\circ\text{C}$ ) for 1 h in HCl 3.5 N and 1 h in  $\text{HNO}_3$  1N (Koppers et al. 2000). Feldspars were leached at room temperature in an ultrasonic bath for a few minutes. A longer leaching time (20 min) was used for alkali feldspar 8.88–9.02 mbsf, because of the presence of melt inclusions. After leaching, samples were washed in ultraclean water and dried on a hot plate at  $\sim 70^\circ\text{C}$ . Splits of a few to several tens of milligrams of feldspars and groundmasses were wrapped in aluminium foil to form discs  $< 9$  mm in diameter and a few millimetres thick. Discs were stacked in pancake fashion within a quartz vial 9 mm in diameter. The stack was interspersed with splits of the standard Fish Canyon sanidine (FCs), every 4–6 mm to monitor the vertical neutron flux.  $J$  values for each stack position were monitored by analyzing 5 single crystals of FCs (assumed age 28.03 Ma, Jourdan and Renne 2007). Samples were irradiated in three distinct batches, for 5 h (PAV–64), 2 h (PAV–65) and 3 h (PAV–66), in the core of the TRIGA reactor at the University of Pavia (Italy).  $^{40}\text{Ar}$ – $^{39}\text{Ar}$  analyses were carried out using different laser extraction techniques and different laserprobes: (1) laser total fusion analysis of single or multi-grain splits of K-rich alkali feldspar using a  $\text{CO}_2$  laser; (2) laser step-heating analysis using either a defocused Nd-doped yttrium-aluminium-garnet (Nd:YAG) laser (for groundmasses) or a defocused  $\text{CO}_2$  laser (feldspars). After irradiation, splits consisting of one to a few grains of alkali feldspars (a few milligrams for total fusion analyses to a few tens of milligrams for step-heating analysis were used only for sample 8.88–9.02 mbsf) to a few tens of milligrams for plagioclase and groundmasses, were placed in 1.5- to 9-mm diameter holes (depending on the sample mass) of a copper holder and baked overnight. Total fusion analyses on alkali feldspars (including the fluence monitor FCs) were carried out using a continuous wave  $\text{CO}_2$  laser defocused to 1 mm spot size. Step-heating analyses of groundmasses were performed using a continuous wave diode-pumped Nd:YAG laser, which was defocused to a 2 mm spot size and slowly rastered (at  $0.1 \text{ mm s}^{-1}$ ) over the grains by a computer-controlled x–y stage to ensure even heating. One plagioclase and one alkali feldspar concentrates were incrementally heated using the  $\text{CO}_2$  laser defocused to 3 mm spot size, which was manually rastered over the

grains to ensure even heating. Step-heating analyses were preceded by a total fusion analysis of mg-splits of the same separate in order to estimate a preliminary age then used to calculate the optimal sample weight for the step-heating run.

After cleanup (8–10 min, including 1 min of lasering for total fusion analyses and 15–20 min for step-heating experiments, including 8–9 min of lasering), using two Saes AP10 getters held at 400°C and one C-50 getter held at room temperature, extracted gases were equilibrated by automated valves into a MAP215–50 noble gas mass spectrometer fitted with a Balzers SEV217 secondary electron multiplier. Ar isotope peak intensities were measured ten times for a total of ~25 min. Blanks were analyzed every one to three analyses. Mass discrimination was monitored by analysis of air pipettes. At the time of data collection mean values were:  $1.0051 \pm 0.0030$  ( $\pm 2\text{SD}$ ,  $n=33$ ) per atomic mass unit (AMU) for PAV–64,  $1.0037 \pm 0.0016$  ( $\pm 2\text{SD}$ ,  $n=13$ ) AMU for PAV–65, and  $1.0038 \pm 0.0018$  ( $\pm 2\text{SD}$ ,  $n=22$ ) AMU for PAV–66. Correction factors for interfering isotopes, determined on K- and Ca-rich glasses, were:  $(^{40}\text{Ar}/^{39}\text{Ar})_{\text{K}}=0.0093$ ,  $(^{38}\text{Ar}/^{39}\text{Ar})_{\text{K}}=0.0129$ ,  $(^{39}\text{Ar}/^{37}\text{Ar})_{\text{Ca}}=0.00075$  and  $(^{36}\text{Ar}/^{37}\text{Ar})_{\text{Ca}}=0.00024$ . Data reduction was performed using the ArArCALC software (Koppers, 2002). Errors are given at  $2\sigma$  and are quoted as: (1) analytical errors, including in-run statistics and uncertainties in the discrimination factor, interference corrections and procedural blanks; (2) internal errors, also including uncertainties in the  $J$  value; (3) full errors, also including uncertainties on the age of the flux monitor and those in the  $^{40}\text{K}$  decay constants. Data corrected for post-irradiation decay, mass discrimination effects, isotopes derived from interference reactions and blanks are listed in Table S1. Ages listed in Table S1 were calculated using the IUGS recommended constants (Steiger and Jäger 1977). More details on the analytical procedures can be found in Di Vincenzo and Skála (2009). Error-weighted means and least squares fits were calculated using v. 3.00 of the Isoplot/Ex program (Ludwig 2003).

## 2. Features of dated rocks

Lithostratigraphic Unit 1 (0 – 37.01 mbsf)

Five samples, consisting of vesiculated lava clasts up to a few centimetres in size, were selected from the Lithostratigraphic Unit 1. A comprehensive description of these samples have been reported by Del Carlo et al. (2009) and will be only summarized here. Sample 8.88–9.02 (a fresh phonolite lava, Fig. S2a) is a lava clast that belongs to the first interval of the core recovered as loose samples in composite bags (bagged samples, i.e. the stratigraphic relationships are not recognizable). It is a fresh subangular glomeroporphyritic lava clast of phonolitic composition containing cm-sized anhedral anorthoclase (Fig. S3) phenocrysts with large glass inclusions (up to 0.5 mm), subhedral medium-grained phenocrysts of zoned clinopyroxene and minor olivine, set in an almost opaque glassy vesiculated groundmass. Flattened vesicles and elongated phenocrysts define a flowage texture.

Sample 10.22–10.44 is a variably vesiculated (5–20%) basanitic lava clast (Fig. S2b) characterized by a phenocrystic assemblage of euhedral skeletal olivine up to 4 mm in length and minor clinopyroxene in a brown glassy groundmass with microlites of clinopyroxene, plagioclase and oxides. Vesicles are irregular in shape and the groundmass consists of patches and streaks of a black to almost opaque glass (i.e., tachylite).

Sample 12.23–12.41 is a glomeroporphyritic vesiculated hawaiitic lava clast characterized by phenocrysts of zoned clinopyroxene (pale-green core to purple-brown rim) and minor olivine in a glassy groundmass that includes microlites of plagioclase, clinopyroxene and magnetite (Fig. S2c). The millimeter-sized rounded vesicles are partially filled with secondary calcite.

The hawaiitic lava clast 18.03–18.25 contains rounded vesicles and phenocrysts of zoned clinopyroxene and minor altered olivine in a glassy groundmass that includes microlites of clinopyroxene, plagioclase and oxides (Fig. S2d).

Sample 18.69–18.73 is a vesiculated (20%) lava clast with a subrounded shape. It is tephritic in composition and contains phenocrysts of clinopyroxene and minor bowlingitic olivine (Fig. S2e).

#### Lithostratigraphic Unit 4 (122.86 – 224.82 mbsf)

Samples 127.50–127.52 and 129.96–129.97 are two clasts from a diamictite, which is the main lithofacies of Lithostratigraphic Unit 4 (Fielding et al. 2008).

Sample 127.50–127.52 is 1 x 2 centimeter-sized subangular lava clast, consisting of a subaphyric trachyte (Fig. S2f) with scattered anorthoclase (Fig. S3) and green pyroxene microphenocrysts set in a trachytic-textured groundmass made of alkali feldspars and magnetite.

Sample 129.96–129.97 is a 1 x 3 centimeter-sized subangular porphyritic (15 vol%) basaltic lava clast with ~1 mm-sized phenocrysts of plagioclase, clinopyroxene and olivine pseudomorphs. The groundmass is made up of plagioclase microlites, altered glass and minor opaque minerals (Fig. S2g).

#### Lithostratigraphic Unit 7 (339.92 – 436.18 mbsf)

Sample 358.11–358.13 is a purplish to dark-brown, a few centimeters wide lava clast from a diamictite level. Euhedral magnetite phenocrysts and tiny plagioclase microphenocrysts, which define a pilotaxitic texture, are set in a holocrystalline groundmass with plagioclase, clinopyroxene, magnetite and apatite (Fig. S2h).

#### Lithostratigraphic Unit 8 (436.18 – 607.35)

Sample 440.83–440.86 is a 5 x 4 centimeter-sized, dark-brown to red, vesicular (15–20 vol%), poorly porphyritic (<1%), intermediate lava clast from a mudstone layer, with



microphenocrysts of plagioclase, abundant magnetite and alkali feldspar in a moderately altered holocrystalline groundmass (Fig. S2i).

Sample 564.92–564.93 is a grey, non-vesicular, porphyritic (10-15 vol%) felsic lava clast from a sandy conglomerate, with phenocrysts of alkali feldspar (~10 vol%), aegirinic clinopyroxene and minor magnetite set in a fine-grained holocrystalline groundmass. The groundmass contains plagioclase, alkali feldspar (mainly anorthoclase in composition, Fig. S3), clinopyroxene and magnetite.

#### Lithostratigraphic Unit 9 (607.35 – 648.74 mbsf)

Sample 640.13–640.16 belongs to a six-centimeter thick normally graded primary pyroclastic deposit within a sandstone interval and consists of grayish fine pumice lapilli to coarse ash. The pumice clasts are aphyric but in rare instances contain phenocrysts of alkali feldspar (mainly anorthoclase in composition, Fig. S3), the latter commonly found as isolated crystal fragments crystals up to ~0.5 mm in size (Fig. S2k). The pumice have very low alkali, magnesium and iron content pointing to a high degree of alteration (Panter et al., 2008). Pumice from the lapilli tuff are set in a fine-grained matrix of volcanic ash of the same chemical composition. Rare siliciclastic fragments (rounded quartz and lithic fragments) are also found. These observations, coupled with the gradational top and the loaded base of the layer, suggest that the deposit formed by direct sinking of a subaerial pyroclastic fallout (Panter et al., 2008).

#### Lithostratigraphic Unit 10 (648.74 – 778.34 mbsf)

Sample 709.14–709.16 and 709.17–709.19 are two similar ~3.5-cm thick layers made of rounded fine pumice lapilli, concentrated along ripple foresets. Pumice are subaphyric (with rare anorthoclase phenocrysts, Fig. S3) whose variably flattened vesicles are filled with calcite (Fig. S2l). Within the pumice clasts a significant amount of foreign detritus is present. Subangular to angular monomineralic clasts (up to ~0.3 mm in size) are represented by quartz, plagioclase, minor microcline and subordinate biotite and amphibole. The lithic component is dominated by volcanic clasts (orange-brownish, vesiculated sideromelane, minor tachylite and holocrystalline very fine-grained holocrystalline porphyritic lava). On the basis of lithological features, these deposits are interpreted as two pyroclastic fall events that settled through the water column to the seafloor and were then reworked by shallow water, wave-base processes.

#### Lithostratigraphic Unit 11 (778.34 – 904.66 mbsf)

Sample 831.66–831.68 represents the thickest (~1 cm thick) of three intervals in Lithostratigraphic Unit 11, where pumice clasts are concentrated. This clast-rich layer, in which the main component is represented by up to 4 mm-sized pumice, has gradational top and bottom contacts within a silty sandstone, which indicates a very weak reworking of a

pyroclastic fall deposit. Monomineralic fragments (alkali feldspar, plagioclase and minor quartz) along with lithic (mostly porphyritic volcanic) clasts also occur (Fig. S2m).

#### Lithostratigraphic Unit 12 (904.66 – 996.69 mbsf)

The analyzed samples from Lithostratigraphic Unit 12 represent two out of the six accumulations ranging from 2 to 10 cm thick (from the 953–964-mbsf interval) of yellow-grey pumices mixed with dark green highly angular clasts dispersed in a muddy fine-grained sandstone. The pumiceous layer of sample 953.28–953.31 (Fig. S2n) is made up of medium- to coarse-grained pumice fragments and also contains single crystals of euhedral anorthoclase (commonly broken) (Fig. S3), subordinate quartz and plagioclase as well as porphyritic pilotaxitic fragments (up to 1–2 mm sized). In sample 953.54–953.56, which is similar in overall composition to the former, pumices are concentrated in a ~1 cm-thick irregular strip and the amount of monomineralic sialic fragments is lower. Pumice are more altered with respect to those of the previous deposits, nevertheless the lack of foreign detritus in the matrix indicates that the pumice accumulations represent nearly primary tephra layers formed by pyroclastic activity.

#### Lithostratigraphic Unit 14 (1040.28 – 1138.54 mbsf)

The lowermost lithostratigraphic unit consists of sandy diamictite and sandstone with dispersed clasts. Sample 1093.00–1093.04 was taken from a 6 cm-thick interval pumice-rich layer that shows sharp, highly angular to crenulated contacts with the surrounding sandstone. It is formed of dense non-vesicular glassy lense-shaped pumice clasts, subangular fresh monomineralic fragments [anorthoclase (Fig. S3), quartz and plagioclase] and felty to pilotaxitic textured volcanic clasts (Fig. S2o). The dark colour of the sample is due to the almost opaque matrix. Individual pumice are altered and replaced similarly to sample 953.54–953.56 and vary in colour from black to dark-green to brown. This layer is mostly matrix-supported, however, there are local areas where lense-shaped pumices are in contact and are imbricated. Foreign detritus is scarce. On the basis of the described features, this deposit represents a pyroclastic event that was very weakly reworked and later intruded by intra-formational sands (e.g., clastic dike-like).

## References

Del Carlo P, Panter KS, Bassett K, Bracciali L, Di Vincenzo G, Rocchi S. (2009) Evidence for local volcanic sources in the upper lithostratigraphic unit of ANDRILL AND-2A core (Southern McMurdo Sound, Antarctica) and implications for paleoenvironment and subsidence in the western Victoria Land basin. *Global Planet Change*. doi: 10.1016/j.gloplacha.2009.09.002

- Di Vincenzo G, Skála R (2009)  $^{40}\text{Ar}$ – $^{39}\text{Ar}$  laser dating of tektites from the Cheb Basin (Czech republic): Evidence for coevality with moldavites and influence of the dating standard on the age of the Ries impact. *Geochim Cosmochim Acta*, 73:493–513
- Fielding CR, Atkins CB, Bassett KN, Browne GH, Dunbar GB, Field BD, Frank TD, Panter KS, Pekar SF, Krissek LA, Passchier S (2008) Sedimentology and stratigraphy of the AND-2A core, ANDRILL Southern McMurdo Sound, Project, Antarctica. In: Harwood DM, Florindo F, Talarico F, Levy RH (eds), *Studies from the ANDRILL, Southern McMurdo Sound Project, Antarctica*. *Terra Antarctica*, 15 (in press)
- Jourdan F, Renne PR (2007) Age calibration of the Fish Canyon sanidine  $^{40}\text{Ar}/^{39}\text{Ar}$  dating standard using primary K–Ar standard. *Geochim Cosmochim Acta* 71:387–402
- Koppers AAP (2002) ArArCALC—software for  $^{40}\text{Ar}/^{39}\text{Ar}$  age calculations. *Comp Geosci* 28:605–619
- Koppers AAP, Staudigel H, Wijbrans JR (2000) Dating crystalline groundmass separates of altered Cretaceous seamount basalts by the  $^{40}\text{Ar}/^{39}\text{Ar}$  incremental heating technique. *Chem Geol* 166:139–158
- Ludwig KR (2003) User's manual for Isoplot 3.00, a geochronological toolkit for Microsoft Excel. Berkeley Geochronology Center Spec Pub, 4:54 pp
- Panter KS, Talarico F, Bassett K, Del Carlo P, Field B, Frank T, Hoffman S, Kuhn G, Reichelt L, Sandroni S, Tavini M, Bracciali L, Cornamusini G, von Eynatten H, Rocchi R (2008) Petrologic and Geochemical Composition of the AND-2A Core, ANDRILL Southern McMurdo Sound Project, Antarctica. In: Harwood DM, Florindo F, Talarico F, Levy RH (eds), *Studies from the ANDRILL, Southern McMurdo Sound Project, Antarctica*. *Terra Antarctica*, 15 (in press)
- Steiger RH, Jäger E (1977) Subcommittee on Geochronology: convention on the use of decay constants in geo- and cosmochronology. *Earth Planet Sci Lett* 36:359–362

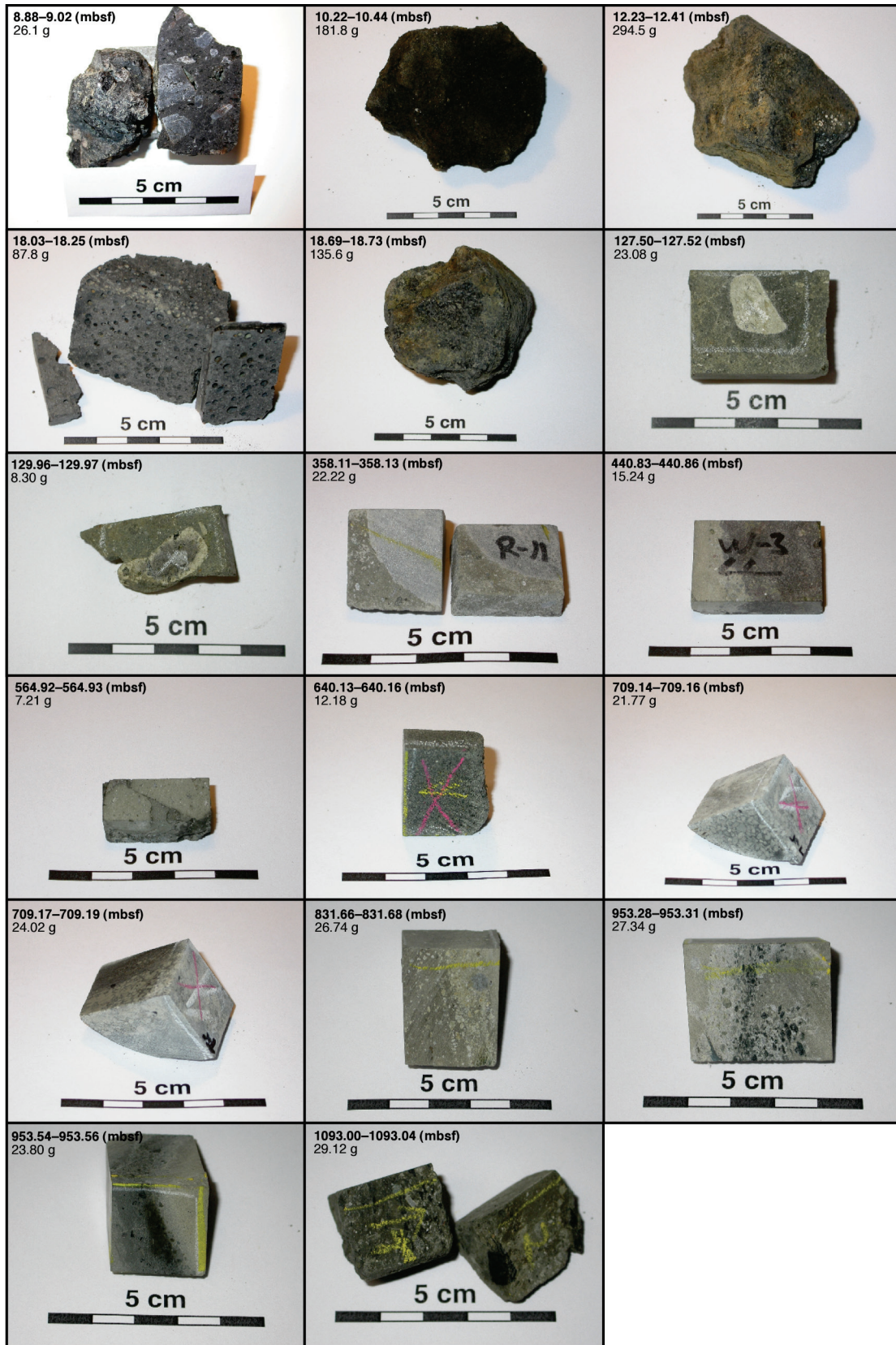
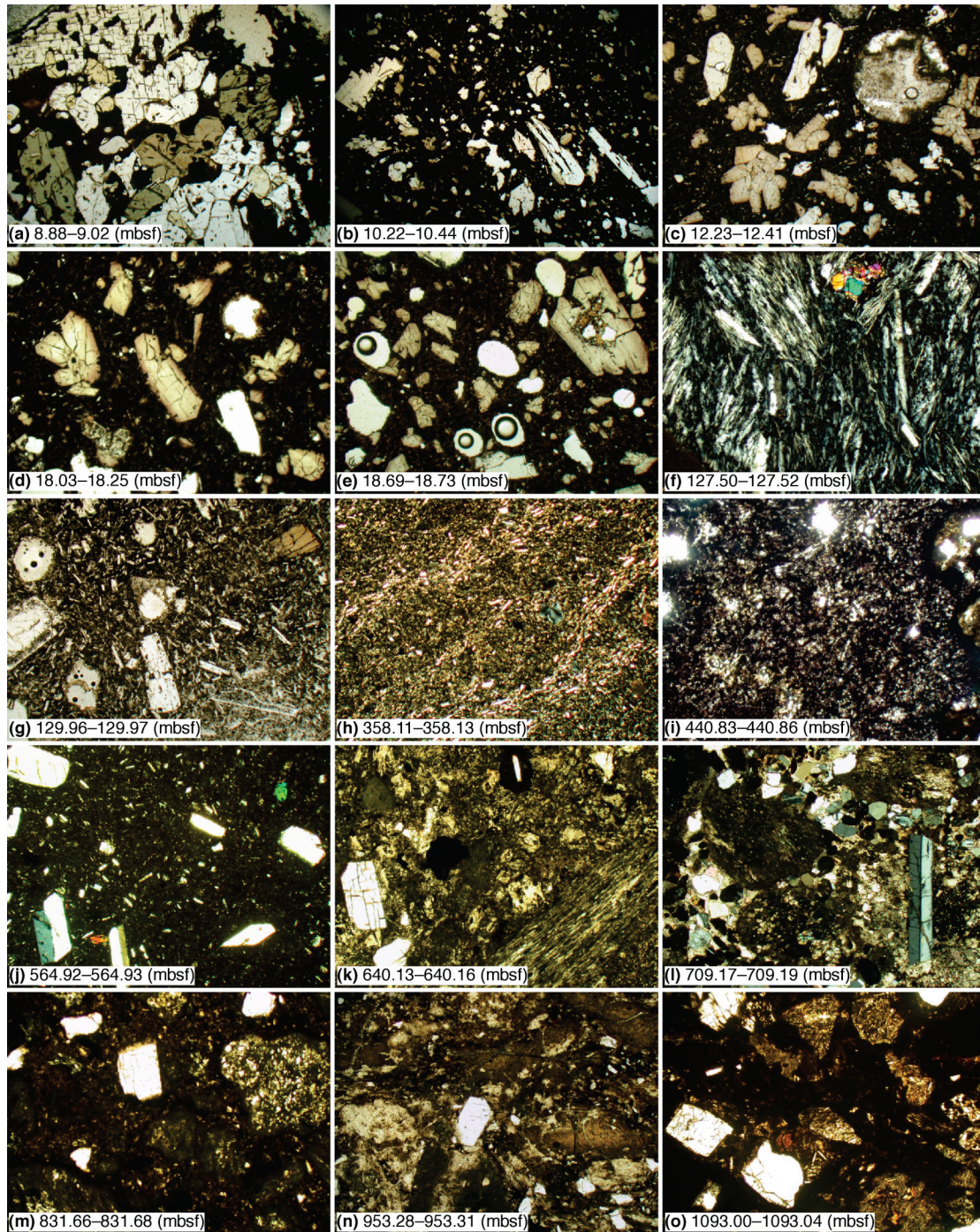
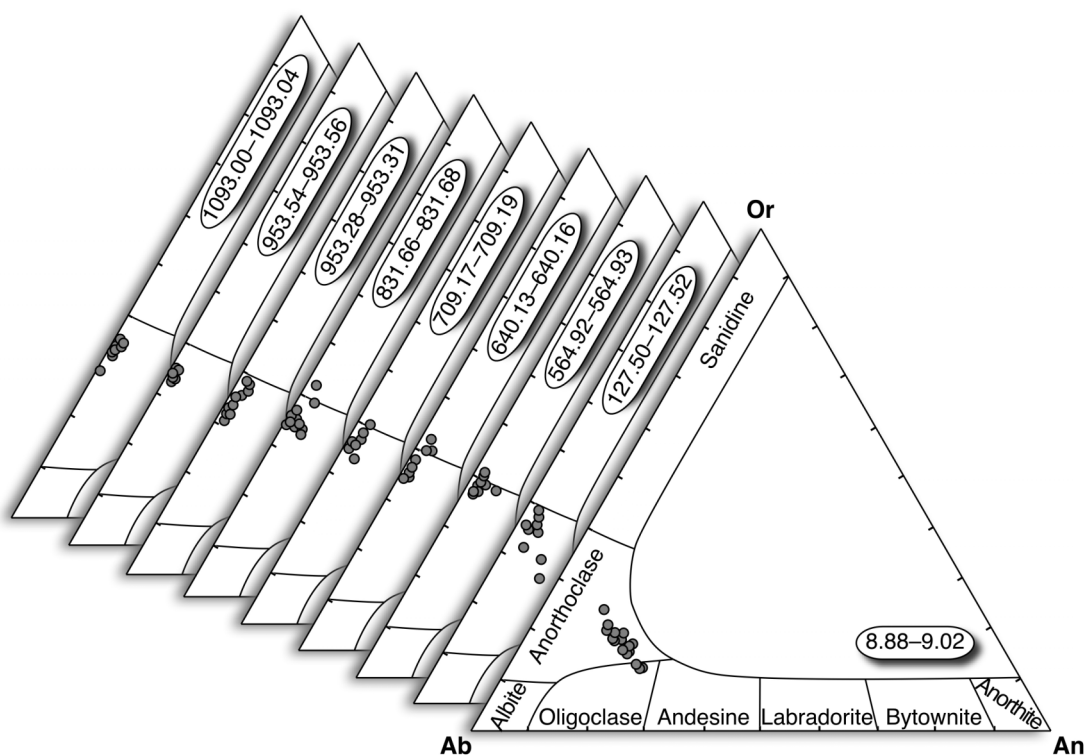


Fig. S1 Photographs showing samples selected for  $^{40}\text{Ar}$ – $^{39}\text{Ar}$  dating before processing.



**Fig. S2** Microphotographs showing the main petrographical features of samples selected for  $^{40}\text{Ar}$ - $^{39}\text{Ar}$  dating from the AND-2A core. **a** sample 8.88–9.02, phonolite lava clast with phenocrysts of coarse-grained alkali feldspar, medium-grained pale-green clinopyroxene and minor yellowish olivine set in an almost opaque groundmass, plane polarized light (PPL), field of view 5.5 mm. **b** sample 10.22–10.44, basanite lava clast with a phenocrystic assemblage of euhedral skeletal olivine and minor pale-brown clinopyroxene in a dark brown glassy groundmass, PPL, field of view 6 mm. **c** sample 12.23–12.41, hawaiite lava clast with glomeroporphyritic clusters of zoned (pale-green core to purple brown rim) clinopyroxene and minor olivine; the rounded vesicle (top-right of image) is partially filled with secondary calcite; PPL, field of view 3 mm. **d** sample 18.03–18.25, hawaiite lava clast with phenocrysts of zoned clinopyroxene and minor altered olivine in a glassy groundmass, PPL, field of view 3 mm. **e** sample 18.69–18.73, vesiculated tephrite lava clast containing phenocrysts of clinopyroxene and minor bowlingitic olivine; note the piroxene with a glassy core (top-right corner of image), PPL, field of view 5 mm. **f** sample 127.50–127.52, trachyte lava clast, with scattered alkali feldspar and minor green pyroxene (top-center) microphenocrysts set in a trachytic-textured groundmass made of alkali feldspars and magnetite, crossed polarized light (CPL), field of view 2 mm. **g** sample 129.96–129.97, basaltic lava clast with phenocrysts of plagioclase, clinopyroxene (top-right) and olivine pseudomorphs (center of

image), PPL, field of view 4 mm. **h** sample 358.11–358.13, euhedral magnetite phenocrysts and tiny plagioclase microphenocrysts define a pilotaxitic alignment in this basaltic lava clast, CPL, field of view 5.5 mm. **i** sample 440.83–440.86, vesicular poorly porphyritic intermediate lava clast with microphenocrysts of plagioclase, abundant magnetite and minor alkali feldspar in a moderately altered holocrystalline groundmass, PPL, field of view 3 mm. **j** sample 564.92–564.93, felsic lava clast with euhedral phenocrysts of alkali feldspar, aegirinic clinopyroxene and minor magnetite, CPL, field of view 5.5 mm. **k** sample 640.13–640.16, pyroclastic deposit containing angular vesiculated pumices (bottom-right of image), rarely with phenocrysts of alkali feldspar, the latter commonly found as isolated crystal fragments crystals (left of image), PPL, field of view 3 mm. **l** sample 709.17–709.19, coarse-grained pumiceous sandstone with a carbonatic cement found within a pumice- rich layer, note the three subaphyric pumices and the alkali feldspar (right), CPL, field of view 3 mm. **m** sample 831.66–831.68, pumice- rich layer with subordinate monomineralic feldspars grains, PPL, field of view 3 mm. **n** sample 953.28–953.31, pumiceous layer containing monomineralic euhedral alkali feldspar grains (e.g. center of image), PPL, field of view 3 mm. **o** sample 1093.00–1093.04, blocky dense clast, dark due to the almost opaque matrix, with strongly altered pumices, subangular fresh monomineralic feldspars and quartz fragments and felty to pilotaxitic textured volcanic clasts, PPL, field of view 6 mm.



**Fig. S3** K-feldspar–Albite–Anorthite triangular plot showing the compositions of alkali feldspars analyzed by the  $^{40}\text{Ar}$ – $^{39}\text{Ar}$  method.

**Table S1**  $^{40}\text{Ar}$ – $^{39}\text{Ar}$  data of groundmasses and feldspars from volcanic samples of the AND-2A Core (ANDRILL SMS Project). Argon isotope concentrations are  $\times 10^{-15}$  moles.

No.	weight (mg) laser power (W) # grains	$^{36}\text{Ar}_{(\text{atm})}$	$^{37}\text{Ar}_{(\text{Ca})}$	$^{38}\text{Ar}_{(\text{Cl})}$	$^{39}\text{Ar}_{(\text{K})}$	$^{40}\text{Ar}_{(\text{Tot})}$	Age (Ma)	$\pm 2\sigma$	$^{40}\text{Ar}^*$ %	$^{39}\text{Ar}_{\text{K}}$ %	Ca/K	$\pm 2\sigma$
sample 8.88–9.02, anorthoclase grain size 0.30–0.50 mm, irradiation PAV–65, $J=0.0001874\pm 0.0000010$												
Total fusion data data												
*1	3.5 mg	0.01440	1.000	0.00301	1.769	4.827	0.109	0.045	11.8	6.4	1.067	0.060
*2	8.2 mg	0.05453	3.382	0.01481	6.492	18.51	0.125	0.028	12.9	23.7	0.983	0.055
*3	7.0 mg	0.03000	2.543	0.01881	4.771	10.56	0.120	0.022	16.0	17.4	1.006	0.056
*4	8.3 mg	0.09283	3.278	0.01990	6.222	29.91	0.135	0.025	8.3	22.7	0.994	0.056
Total gas age							0.125	0.014				
Error-weighted mean age (4 of 4 steps), MSWD=0.59							0.124	0.014				
isochron age ( $^{36}\text{Ar}/^{40}\text{Ar}$ vs. $^{39}\text{Ar}/^{40}\text{Ar}$ diagram), MSWD=0.89							0.107	0.039				
$^{40}\text{Ar}/^{36}\text{Ar}$ intercept							301	11				
sample 8.88–9.02, anorthoclase grain size 0.30–0.50 mm, 56.3 mg, irradiation PAV–65, $J=0.0001874\pm 0.0000010$												
step-heating data												
1	0.3 W	0.32478	0.609	0.00511	1.382	96.28	0.08	0.35	0.3	3.1	0.832	0.048
2	0.5 W	0.02805	0.782	0.00433	1.428	8.831	0.128	0.094	6.1	3.2	1.033	0.059
3	0.8 W	0.02927	2.243	0.01265	4.113	9.293	0.053	0.022	6.9	9.2	1.029	0.058
4	1.3 W	0.02183	2.799	0.01840	5.337	8.298	0.117	0.014	22.1	11.9	0.990	0.056
5	2.0 W	0.04597	4.388	0.04982	8.624	18.87	0.207	0.013	27.9	19.2	0.960	0.054
6	2.8 W	0.02128	2.243	0.02283	4.313	9.095	0.220	0.026	30.7	9.6	0.981	0.055
7	4.1 W	0.00568	1.554	0.00975	2.893	2.979	0.152	0.022	43.3	6.4	1.013	0.058
8	6.6 W	0.00527	4.550	0.00435	8.244	3.857	0.094	0.013	58.4	18.4	1.041	0.058
9	8.0 W	0.01081	4.685	0.00482	8.460	5.047	0.074	0.011	36.2	18.8	1.045	0.058
10	10 W	0.00557	0.05867	bdl	0.09904	1.661	0.05	0.65	0.8	0.2	1.12	0.13
Total gas age							0.127	0.013				
Error-weighted mean age, no plateau							–	–				
sample 10.22–10.44, groundmass, grain size 0.30–0.50 mm, 50.4 mg, irradiation PAV–64, $J=0.0004490\pm 0.0000040$												
step-heating data												
1	0.20 W	0.01617	0.1139	0.04020	0.1515	5.318	2.9	2.8	10.1	0.2	1.42	0.18
2	0.50 W	0.02453	2.167	0.8095	3.489	11.34	0.95	0.15	36.0	5.6	1.172	0.071
*3	0.70 W	0.01130	3.031	1.132	5.214	8.069	0.735	0.080	58.3	8.4	1.097	0.067
*4	0.90 W	0.01139	3.011	1.058	5.116	7.716	0.689	0.085	56.0	8.3	1.110	0.068
*5	1.2 W	0.4278	6.665	1.772	9.128	134.5	0.72	0.19	6.0	14.8	1.378	0.083
*6	1.5 W	0.1180	16.16	3.238	17.60	49.51	0.674	0.050	29.5	28.4	1.73	0.10
7	1.8 W	0.01514	16.74	1.579	9.013	11.08	0.594	0.035	59.2	14.6	3.50	0.21
8	2.5 W	0.01662	32.72	1.165	6.725	9.387	0.539	0.073	47.4	10.9	9.18	0.56
9	5.5 W	0.02198	96.49	0.7726	4.626	9.229	0.48	0.26	29.5	7.5	39.4	2.4
10	15 W	0.00925	45.40	0.1383	0.8167	2.990	0.25	0.77	8.5	1.3	104.9	6.5
Total gas age							0.662	0.042				
Error-weighted mean age (4 out of 10 steps), MSWD=0.59							0.692	0.038	59.9			
isochron age ( $^{36}\text{Ar}/^{40}\text{Ar}$ vs. $^{39}\text{Ar}/^{40}\text{Ar}$ diagram), MSWD=0.89							0.691	0.047				
$^{40}\text{Ar}/^{36}\text{Ar}$ intercept							295.7	5.5				
sample 12.23–12.41, groundmass, grain size 0.30–0.50 mm, 52.1 mg, irradiation PAV–64, $J=0.0004524\pm 0.0000039$												
step-heating data												
1	0.20 W	0.03455	0.1329	0.04024	0.1656	10.50	1.4	2.7	2.8	0.8	1.51	0.16
2	0.50 W	0.1205	3.773	0.5334	3.390	40.88	1.27	0.30	12.9	16.0	2.10	0.13
*3	0.70 W	0.03368	5.422	0.4906	3.328	13.13	0.78	0.10	24.2	15.7	3.07	0.19

**Table S1** Continued

No.	# grains weight (mg) laser power (W)	<sup>36</sup> Ar <sub>(atm)</sub>	<sup>37</sup> Ar <sub>(Ca)</sub>	<sup>38</sup> Ar <sub>(Cl)</sub>	<sup>39</sup> Ar <sub>(K)</sub>	<sup>40</sup> Ar <sub>(Tot)</sub>	Age (Ma)	±2σ	<sup>40</sup> Ar* %	<sup>39</sup> Ar <sub>K</sub> %	Ca/K	±2σ
*4	0.90 W	0.02401	5.292	0.5356	3.729	10.76	0.801	0.080	33.9	17.6	2.68	0.16
5	1.2 W	0.03069	4.229	0.5670	3.714	11.96	0.634	0.078	24.1	17.6	2.15	0.14
6	1.5 W	0.03297	7.308	0.4157	2.643	11.95	0.68	0.15	18.5	12.5	5.22	0.32
7	1.8 W	0.02577	19.31	0.3731	2.319	9.026	0.50	0.19	15.6	11.0	15.7	1.0
8	2.5 W	0.01595	30.39	0.2187	1.249	5.219	0.33	0.37	9.6	5.9	45.9	2.8
9	5.0 W	0.01256	58.68	0.07965	0.4316	3.834	0.2	1.7	3.2	2.0	257	17
10	15 W	0.01204	69.03	0.02714	0.1709	3.649	0.4	5.7	2.5	0.8	762	69
Total gas age							0.758	0.090				
Error-weighted mean age, no plateau							0.793	0.062	33.4			
sample 18.03–18.25, groundmass, grain size 0.30–0.50 mm, 1.6 mg, irradiation PAV–64, J=0.0004551±0.0000032												
Total fusion data												
1	15 W	0.4074	9.471	0.1034	0.6397	133.2	16.1	2.2	9.6	–	27.9	1.8
sample 18.69–18.73, groundmass, grain size 0.30–0.50 mm, 2.5 mg, irradiation PAV–64, J=0.0004579±0.0000028												
Total fusion data												
1	15 W	0.5748	8.960	0.3159	1.655	189.2	9.5	1.2	10.2	–	10.21	0.64
sample 127.50–127.52, alkali feldspar, grain size >0.25 mm, irradiation PAV–64, J=0.0004590±0.0000028												
Total fusion data												
*1	1	0.00688	0.04639	bdl	1.952	28.76	11.30	0.15	92.9	3.8	0.0448	0.0070
*2	1	0.02792	0.50067	0.00272	9.131	133.7	11.345	0.049	93.8	17.7	0.1035	0.0058
*3	1	0.00353	0.13080	0.00026	5.087	71.10	11.368	0.069	98.5	9.9	0.0485	0.0030
*4	2	0.00240	0.09199	0.00044	4.365	60.91	11.385	0.071	98.8	8.5	0.0398	0.0028
*5	3	0.00333	0.13593	bdl	3.567	49.99	11.341	0.080	98.0	6.9	0.0719	0.0049
*6	5	0.00463	0.08861	0.00033	2.731	38.70	11.284	0.096	96.4	5.3	0.0612	0.0040
*7	1	0.01299	0.15140	bdl	5.419	78.34	11.350	0.069	95.0	10.5	0.0527	0.0032
*8	1	0.02048	0.11028	0.00022	3.807	58.32	11.334	0.096	89.6	7.4	0.0547	0.0039
9	3	0.03539	0.11703	0.00042	3.217	55.38	11.53	0.11	81.1	6.3	0.0686	0.0047
*10	7	0.00140	0.03789	bdl	1.313	18.50	11.37	0.19	97.7	2.6	0.0544	0.0078
*11	5	0.00328	0.02601	0.00069	0.9377	13.78	11.27	0.26	92.9	1.8	0.052	0.010
*12	1	0.01629	0.23925	0.00416	9.924	142.0	11.414	0.048	96.5	19.3	0.0455	0.0034
Total gas age							11.369	0.072				
Error-weighted mean age (11 of 12 runs), MSWD=1.65							11.363	0.072				
isochron age ( <sup>36</sup> Ar/ <sup>40</sup> Ar vs. <sup>39</sup> Ar/ <sup>40</sup> Ar diagram), MSWD=1.48							11.347	0.080				
<sup>40</sup> Ar/ <sup>36</sup> Ar intercept							307	16				
sample 129.96–129.97, plagioclase, grain size 0.30–0.50 mm, 34.0 mg, irradiation PAV–64, J=0.0004597±0.0000028												
step-heating data												
*1	0.3 W	14.48	6.168	0.05097	0.3838	4285	10	115	0.1	9.4	30.3	2.7
*2	0.5 W	2.171	16.62	0.01193	0.3622	648.5	16	18	1.1	8.9	86.6	5.4
*3	0.8 W	0.4166	34.79	0.03193	0.6014	131.1	11.0	2.5	6.1	14.8	109.2	6.9
*4	1.3 W	0.04836	24.14	0.00715	0.5783	22.07	11.1	1.2	35.2	14.2	78.8	4.9
*5	2.0 W	0.04464	17.58	0.00511	0.4645	19.61	11.4	1.5	32.7	11.4	71.4	4.5
*6	3.3 W	0.12520	27.29	0.00602	0.8263	49.30	12.3	1.0	24.9	20.3	62.3	3.9
*7	4.3 W	0.01032	12.77	0.00198	0.3562	7.953	11.38	0.81	61.6	8.8	67.6	4.2
*8	10 W	0.01470	28.46	0.00150	0.4904	10.86	10.98	0.98	60.0	12.1	109.5	6.9
Total gas age							12	11				
Error-weighted mean age (8 of 8 steps), MSWD=0.63							11.43	0.46	100.0			



**Table S1** Continued

No.	# grains weight (mg) laser power (W)	<sup>36</sup> Ar <sub>(atm)</sub>	<sup>37</sup> Ar <sub>(Ca)</sub>	<sup>38</sup> Ar <sub>(Cl)</sub>	<sup>39</sup> Ar <sub>(K)</sub>	<sup>40</sup> Ar <sub>(Tot)</sub>	Age (Ma)	±2σ	<sup>40</sup> Ar* %	<sup>39</sup> Ar <sub>K</sub> %	Ca/K	±2σ
isochron age ( <sup>36</sup> Ar/ <sup>40</sup> Ar vs. <sup>39</sup> Ar/ <sup>40</sup> Ar diagram), MSWD=0.71							11.39	0.49				
<sup>40</sup> Ar/ <sup>36</sup> Ar intercept							296.0	2.3				
sample 358.11–358.13, groundmass, grain size 0.30–0.50 mm, 26.0 mg, irradiation PAV–66, J=0.0002761±0.0000011												
step-heating data												
1	0.15 W	0.0425	0.1996	0.00285	0.09441	16.68	21.7	2.5	24.8	0.3	3.99	0.29
2	0.30 W	0.0832	1.864	0.00583	1.610	90.89	20.40	0.18	72.9	5.3	2.19	0.12
3	0.45 W	0.0564	3.460	0.00064	4.745	172.6	16.299	0.089	90.3	15.6	1.376	0.076
*4	0.55 W	0.0247	2.882	0.00050	4.295	145.6	15.965	0.065	95.0	14.1	1.266	0.069
*5	0.70 W	0.0172	2.895	0.00147	4.508	149.4	15.877	0.081	96.6	14.8	1.212	0.066
*6	0.85 W	0.0139	2.193	0.00214	3.617	120.2	15.921	0.062	96.5	11.9	1.144	0.063
*7	1.0 W	0.0122	1.721	0.00084	2.589	86.23	15.830	0.091	95.8	8.5	1.255	0.069
8	1.2 W	0.0158	1.838	0.00257	2.277	76.71	15.691	0.090	93.9	7.5	1.523	0.083
9	1.5 W	0.0283	4.671	0.00515	3.373	113.0	15.381	0.082	92.6	11.1	2.61	0.14
10	2.0 W	0.0187	11.05	0.00524	2.150	71.53	15.23	0.11	92.3	7.1	9.69	0.53
11	3.0 W	0.0046	3.550	0.00045	0.3717	12.73	15.15	0.36	89.2	1.2	18.02	0.99
12	6.0 W	0.0043	1.854	bdl	0.1635	5.915	14.06	0.93	78.3	0.5	21.4	1.3
13	15 W	0.0079	4.921	0.00270	0.6012	21.34	15.68	0.26	89.0	2.0	15.44	0.85
Total gas age							16.08	0.14				
Error-weighted mean age (4 out of 13 steps), MSWD=2.23							15.91	0.14		49.4		
isochron age ( <sup>36</sup> Ar/ <sup>40</sup> Ar vs. <sup>39</sup> Ar/ <sup>40</sup> Ar diagram), MSWD=1.81							15.74	0.32				
<sup>40</sup> Ar/ <sup>36</sup> Ar intercept							373	130				
sample 440.83–440.86, feldspars, grain size >0.18 mm, irradiation PAV–66, J=0.0002762±0.0000011												
Total fusion data												
1	1	0.02868	bdl	0.00188	0.8441	935.8	478.1	2.4	99.1	40.3	–	
2	1	0.01993	0.00290	0.00009	0.6835	299.9	202.6	1.8	98.0	32.6	0.008	0.012
*3	1	0.00103	0.00283	0.00020	0.2565	8.701	16.23	0.77	96.5	12.2	0.021	0.034
*4	1	0.00115	0.01055	0.00026	0.2994	10.36	16.60	0.35	96.7	14.3	0.066	0.020
5	1	0.00991	0.04717	0.00008	0.01196	25.48	756	36	88.5	0.6	7.44	0.77
Total gas age							277.7	2.7				
Error-weighted mean age (2 out of 5 runs), MSWD=0.74							16.54	0.34				
sample 564.92–564.93, alkali feldspar, grain size >0.25 mm, irradiation PAV–66, J=0.0002764±0.0000022												
Total fusion data												
*1	1	0.00247	0.03379	0.00024	1.172	41.24	17.15	0.13	98.2	5.6	0.0544	0.0048
*2	1	0.00106	0.00073	0.00011	0.3329	11.81	17.14	0.28	97.3	1.6	0.004	0.018
*3	3	0.00435	0.03915	0.00008	2.150	75.58	17.150	0.071	98.3	10.3	0.0344	0.0036
*4	1	0.00364	0.11080	bdl	1.815	63.64	17.104	0.113	98.3	8.7	0.1152	0.0080
*5	1	0.00252	0.04470	bdl	1.335	46.97	17.19	0.13	98.4	6.4	0.0632	0.0071
*6	1	0.00091	0.01017	bdl	0.6609	22.79	16.91	0.20	98.8	3.2	0.0290	0.0096
*7	3	0.00256	0.01238	0.00036	1.339	47.17	17.20	0.13	98.4	6.4	0.0174	0.0051
*8	3	0.00238	0.01133	bdl	1.021	35.76	17.04	0.14	98.0	4.9	0.0209	0.0062
*9	1	0.00368	0.01569	bdl	0.8246	29.48	17.09	0.14	96.3	3.9	0.0359	0.0065
*10	3	0.00371	0.01851	0.00058	1.438	50.53	17.056	0.098	97.8	6.9	0.0243	0.0049
*11	5	0.00424	0.03978	0.00036	1.776	62.61	17.145	0.092	98.0	8.5	0.0423	0.0044
*12	5	0.00348	0.02656	bdl	2.056	71.95	17.115	0.091	98.5	9.8	0.0244	0.0046
*13	1	0.00213	0.01325	bdl	0.5767	20.59	17.18	0.24	96.9	2.8	0.043	0.012
*14	3	0.00637	0.02152	bdl	1.445	51.64	17.089	0.095	96.3	6.9	0.0281	0.0043

Table S1 Continued

No.	# grains weight (mg) laser power (W)	<sup>36</sup> Ar <sub>(atm)</sub>	<sup>37</sup> Ar <sub>(Ca)</sub>	<sup>38</sup> Ar <sub>(Cl)</sub>	<sup>39</sup> Ar <sub>(K)</sub>	<sup>40</sup> Ar <sub>(Tot)</sub>	Age (Ma)	±2σ	<sup>40</sup> Ar* %	<sup>39</sup> Ar <sub>K</sub> %	Ca/K	±2σ
*15	3	0.00301	0.02043	0.00020	1.188	41.59	16.999	0.083	97.8	5.7	0.0324	0.0056
*16	3	0.00354	0.02802	bdl	1.789	62.50	17.054	0.085	98.3	8.5	0.0296	0.0034
Total gas age							17.11	0.14				
Error-weighted mean age (16 of 16 runs), MSWD=1.37							17.10	0.14				
isochron age ( <sup>36</sup> Ar/ <sup>40</sup> Ar vs. <sup>39</sup> Ar/ <sup>40</sup> Ar diagram), MSWD=1.42							17.07	0.17				
<sup>40</sup> Ar/ <sup>36</sup> Ar intercept							324	86				
sample 640.13–640.16, alkali feldspar, grain size >0.18 mm, irradiation PAV–64, J=0.0004603±0.0000028												
Total fusion data												
*1	1	0.00079	0.00299	bdl	0.3403	7.408	17.42	0.72	96.8	1.4	0.017	0.035
*2	4	0.00099	0.00257	0.00075	1.448	30.78	17.40	0.19	99.0	6.0	0.0033	0.0041
*3	5	0.00225	0.01232	0.00017	1.611	34.48	17.35	0.16	98.0	6.7	0.0144	0.0057
*4	4	0.00506	0.02381	bdl	1.434	31.76	17.44	0.17	95.3	5.9	0.0313	0.0062
*5	5	0.00353	0.00259	0.00095	1.303	28.93	17.69	0.25	96.4	5.4	0.0038	0.0048
*6	5	0.00463	0.01176	bdl	2.389	51.67	17.40	0.13	97.3	9.9	0.0093	0.0030
*7	10	0.00374	0.04596	bdl	3.307	70.53	17.351	0.092	98.4	13.7	0.0262	0.0028
*8	5	0.00131	0.00462	0.00010	1.053	22.57	17.41	0.24	98.2	4.4	0.0083	0.0081
*9	7	0.00217	0.02690	0.00071	1.518	32.49	17.34	0.17	98.0	6.3	0.0334	0.0054
*10	5	0.00217	0.03239	0.00000	1.883	40.26	17.39	0.17	98.4	7.8	0.0325	0.0050
*11	5	0.01272	0.01328	0.00056	1.182	29.33	17.87	0.30	87.2	4.9	0.0212	0.0083
*12	5	0.00238	0.01157	0.00047	1.114	24.02	17.30	0.18	97.0	4.6	0.0196	0.0082
*13	5	0.00101	0.00823	0.00027	1.226	26.13	17.41	0.14	98.8	5.1	0.0127	0.0086
*14	1	0.00120	0.02422	0.00014	0.3461	7.676	17.48	0.67	95.3	1.4	0.132	0.041
*15	6	0.00030	0.01784	0.00074	1.607	33.81	17.34	0.14	99.7	6.7	0.021	0.010
*16	4	0.00150	0.01011	0.00008	0.9866	20.97	17.20	0.26	97.8	4.1	0.019	0.025
*17	7	0.00150	0.01610	bdl	1.385	29.52	17.35	0.16	98.5	5.7	0.022	0.011
Total gas age							17.41	0.11				
Error-weighted mean age (17 of 17 runs), MSWD=1.39							17.39	0.11				
isochron age ( <sup>36</sup> Ar/ <sup>40</sup> Ar vs. <sup>39</sup> Ar/ <sup>40</sup> Ar diagram), MSWD=0.49							17.30	0.12				
<sup>40</sup> Ar/ <sup>36</sup> Ar intercept							360	40				
sample 709.14–709.16, alkali feldspar/plagioclase, grain size >0.18 mm, irradiation PAV–64, J=0.0004614±0.0000028												
Total fusion data												
*1	1	0.03840	0.02621	0.00029	0.4404	21.03	18.21	0.77	46.0	11.8	0.112	0.027
*2	3	0.00232	0.01684	0.00002	1.0655	24.06	18.17	0.24	97.1	28.5	0.030	0.007
*3	3	0.00346	0.10423	0.00151	1.2331	27.91	18.06	0.21	96.3	33.0	0.159	0.012
4	3	0.00950	0.01957	0.00068	0.2263	19.74	61.2	1.7	85.8	6.1	0.163	0.041
5	3	0.00589	0.14108	0.00109	0.1172	4.699	20.9	2.0	63.0	3.1	2.27	0.15
6	3	0.02189	0.15972	0.00088	0.00707	8.645	239	42	25.2	0.2	42.6	5.9
*7	2	0.00442	0.02573	bdl	0.1848	5.517	18.9	1.0	76.3	4.9	0.263	0.063
*8	1	0.00002	0.00377	0.00071	0.1355	3.041	18.5	1.1	99.7	3.6	0.052	0.093
*9	2	0.00194	0.00183	0.00025	0.1204	3.306	18.8	1.2	82.6	3.2	0.029	0.084
10	2	0.00155	0.01106	0.00028	0.2047	5.387	19.93	0.79	91.5	5.5	0.102	0.061
Total gas age							21.47	0.25				
Error-weighted mean age (6 out of 10 runs), MSWD=0.95							18.15	0.18				
isochron age ( <sup>36</sup> Ar/ <sup>40</sup> Ar vs. <sup>39</sup> Ar/ <sup>40</sup> Ar diagram), MSWD=1.09							18.13	0.20				
<sup>40</sup> Ar/ <sup>36</sup> Ar intercept							299	12				

Table S1 Continued

No.	# grains weight (mg) laser power (W)	<sup>36</sup> Ar <sub>(atm)</sub>	<sup>37</sup> Ar <sub>(Ca)</sub>	<sup>38</sup> Ar <sub>(Cl)</sub>	<sup>39</sup> Ar <sub>(K)</sub>	<sup>40</sup> Ar <sub>(Tot)</sub>	Age (Ma)	±2σ	<sup>40</sup> Ar* %	<sup>39</sup> Ar <sub>K</sub> %	Ca/K	±2σ
sample 709.17–709.19, alkali feldspar/plagioclase, grain size >0.18 mm, irradiation PAV–64, J=0.0004618±0.0000028												
Total fusion data												
*1	1	0.0102	0.0264	0.0004	0.9096	22.61	17.85	0.31	86.6	30.0	0.055	0.009
	2	0.0060	0.0063	0.0003	0.4819	12.84	19.05	0.56	86.3	15.9	0.025	0.015
	3	0.0106	0.0926	0.0007	0.4147	12.79	19.29	0.64	75.4	13.7	0.421	0.030
	4	0.0012	bdl	bdl	0.2186	5.502	19.5	1.0	93.4	7.2	–	
	5	0.0045	bdl	0.0005	0.0766	10.90	101.3	3.2	87.8	2.5	–	
	6	0.0134	0.2022	0.0004	0.1640	13.60	48.4	1.6	71.0	5.4	2.33	0.15
*7	2	0.0040	0.0004	0.0004	0.1662	4.957	18.8	1.3	76.2	5.5	0.005	0.087
*8	2	0.0012	0.0032	0.0006	0.2395	5.548	17.99	0.80	93.6	7.9	0.025	0.054
*9	2	0.0012	0.0032	0.0002	0.2607	5.962	17.81	0.79	93.9	8.6	0.023	0.053
*10	2	0.0016	0.0006	bdl	0.09820	2.682	18.6	1.3	82.0	3.2	0.01	0.16
Total gas age							22.26	0.28				
Error-weighted mean age (5 out of 10 runs), MSWD=0.83							17.93	0.28				
isochron age ( <sup>36</sup> Ar/ <sup>40</sup> Ar vs. <sup>39</sup> Ar/ <sup>40</sup> Ar diagram), MSWD=0.43							17.44	0.86				
<sup>40</sup> Ar/ <sup>36</sup> Ar intercept							351	92				
sample 831.66–831.68, alkali feldspar, grain size >0.25 mm, irradiation PAV–64, J=0.0004623±0.0000028												
Total fusion data												
*1	1	0.01925	0.00147	bdl	3.252	79.10	18.73	0.12	92.8	13.8	0.0009	0.0024
*2	1	0.00353	0.00523	0.00061	4.039	91.92	18.67	0.09	98.8	17.1	0.0024	0.0023
*3	1	0.00363	0.04793	bdl	1.993	46.04	18.72	0.14	97.6	8.4	0.0454	0.0053
*4	1	0.00303	0.00220	0.00088	1.285	29.75	18.64	0.21	97.0	5.4	0.0032	0.0077
*5	1	0.00232	0.02308	0.00053	1.203	27.98	18.83	0.22	97.5	5.1	0.0362	0.0085
*6	3	0.00246	0.02572	0.00121	1.610	36.80	18.59	0.20	98.0	6.8	0.0301	0.0062
*7	1	0.00456	0.00202	0.00047	1.426	33.33	18.62	0.17	95.9	6.0	0.003	0.011
*8	1	0.00195	bdl	bdl	1.062	24.66	18.82	0.23	97.6	4.5	–	
*9	1	0.00133	0.05870	bdl	1.175	26.89	18.71	0.22	98.5	5.0	0.0943	0.0119
*10	1	0.00131	bdl	0.00053	0.9832	22.57	18.72	0.25	98.2	4.2	–	
*11	1	0.00097	bdl	0.00161	0.8143	18.77	18.83	0.22	98.4	3.5	–	
*12	3	0.00177	0.00090	0.00091	1.668	38.22	18.75	0.15	98.6	7.1	0.0010	0.0144
*13	1	0.00089	0.00330	0.00029	0.4195	9.523	18.32	0.50	97.2	1.8	0.0148	0.0375
*14	3	0.00153	0.00310	0.00019	1.514	34.55	18.69	0.15	98.7	6.4	0.0039	0.0125
*15	3	0.00092	0.00026	0.00004	1.148	26.38	18.88	0.21	98.9	4.9	0.0004	0.0220
Total gas age							18.71	0.12				
Error-weighted mean age (15 of 15 runs), MSWD=0.93							18.71	0.12				
isochron age ( <sup>36</sup> Ar/ <sup>40</sup> Ar vs. <sup>39</sup> Ar/ <sup>40</sup> Ar diagram), MSWD=0.98							18.69	0.13				
<sup>40</sup> Ar/ <sup>36</sup> Ar intercept							304	32				
sample 953.28–953.31, alkali feldspar, grain size >0.25 mm, irradiation PAV–64, J=0.0004629±0.0000028												
Total fusion data												
*1	1	0.01191	0.01684	0.00116	5.079	122.5	19.463	0.092	97.1	10.6	0.0063	0.0013
*2	1	0.02354	0.01757	0.00058	4.670	116.2	19.421	0.084	94.0	9.7	0.0071	0.0020
*3	1	0.00596	0.00630	bdl	2.588	62.16	19.39	0.13	97.1	5.4	0.0046	0.0048
*4	1	0.00596	0.05627	bdl	5.929	140.8	19.484	0.079	98.7	12.3	0.0179	0.0020
*5	1	0.00766	0.00982	0.00044	4.105	98.21	19.413	0.091	97.7	8.5	0.0045	0.0019
*6	1	0.00211	0.02411	0.00131	2.135	50.37	19.35	0.14	98.7	4.4	0.0213	0.0057
*7	1	0.00195	0.00975	bdl	2.454	57.92	19.41	0.15	99.0	5.1	0.0075	0.0051
*8	1	0.00200	0.03461	0.00066	2.022	48.02	19.48	0.15	98.7	4.2	0.0323	0.0064

**Table S1** Continued

No.	# grains weight (mg) laser power (W)	<sup>36</sup> Ar <sub>(atm)</sub>	<sup>37</sup> Ar <sub>(Ca)</sub>	<sup>38</sup> Ar <sub>(Cl)</sub>	<sup>39</sup> Ar <sub>(K)</sub>	<sup>40</sup> Ar <sub>(Tot)</sub>	Age (Ma)	±2σ	<sup>40</sup> Ar* %	<sup>39</sup> Ar <sub>K</sub> %	Ca/K	±2σ
*9	1	0.00371	0.00672	bdl	2.201	52.91	19.56	0.13	97.9	4.6	0.0058	0.0054
*10	1	0.00237	0.00618	0.00111	2.482	59.01	19.51	0.15	98.8	5.2	0.0047	0.0050
*11	1	0.00271	bdl	bdl	2.027	48.07	19.37	0.12	98.3	4.2	–	
*12	5	0.00382	0.03530	bdl	4.360	103.1	19.43	0.10	98.9	9.1	0.0153	0.0028
*13	2	0.00255	0.02238	bdl	3.409	80.63	19.459	0.081	99.0	7.1	0.0124	0.0035
*14	1	0.00169	0.01094	bdl	2.139	50.80	19.53	0.14	99.0	4.5	0.0096	0.0119
*15	1	0.00247	0.02281	0.00052	2.453	57.85	19.34	0.12	98.7	5.1	0.0175	0.0087
Total gas age							19.44	0.12				
Error-weighted mean age (15 of 15 runs), MSWD=1.06							19.44	0.12				
isochron age ( <sup>36</sup> Ar/ <sup>40</sup> Ar vs. <sup>39</sup> Ar/ <sup>40</sup> Ar diagram), MSWD=1.14							19.45	0.13				
<sup>40</sup> Ar/ <sup>36</sup> Ar intercept							292	28				
sample 953.54–953.56, alkali feldspar, grain size >0.25 mm, irradiation PAV–64, J=0.0004640±0.0000028												
Total fusion data												
*1	1	0.00865	0.00404	0.00006	0.7982	21.10	19.34	0.31	87.8	5.7	0.010	0.010
*2	1	0.00387	0.00402	bdl	0.8700	21.57	19.55	0.34	94.7	6.2	0.009	0.008
*3	1	0.00113	0.00238	0.00011	1.050	24.95	19.51	0.27	98.6	7.5	0.004	0.013
*4	1	0.01611	0.09551	0.00117	1.095	30.51	19.57	0.25	84.4	7.9	0.164	0.013
*5	2	0.00159	0.00190	0.00011	1.122	26.61	19.39	0.27	98.2	8.1	0.003	0.008
*6	3	0.00474	0.01119	0.00002	2.601	62.66	19.61	0.14	97.7	18.7	0.008	0.003
*7	1	0.00047	0.00007	0.00070	0.5905	14.13	19.73	0.39	99.0	4.2	0.000	0.023
*8	1	0.00242	0.00246	bdl	0.9783	23.62	19.49	0.22	96.9	7.0	0.005	0.016
*9	1	0.00069	0.00080	bdl	0.8507	20.07	19.44	0.21	98.9	6.1	0.002	0.013
*10	2	0.00631	0.00081	bdl	0.9551	24.00	19.30	0.27	92.2	6.9	0.002	0.011
*11	3	0.00431	0.00862	bdl	1.282	31.03	19.33	0.18	95.9	9.2	0.013	0.008
*12	6	0.00509	0.02140	0.00036	1.726	42.06	19.56	0.21	96.4	12.4	0.023	0.012
Total gas age							19.49	0.14				
Error-weighted mean age (12 of 12 runs), MSWD=1.11							19.49	0.14				
isochron age ( <sup>36</sup> Ar/ <sup>40</sup> Ar vs. <sup>39</sup> Ar/ <sup>40</sup> Ar diagram), MSWD=1.21							19.50	0.15				
<sup>40</sup> Ar/ <sup>36</sup> Ar intercept							293	23				
sample 1093.00–1093.04, alkali feldspar, grain size >0.25 mm, irradiation PAV–64, J=0.0004645±0.0000028												
Total fusion data												
*1	1	0.00860	0.03536	0.00130	3.273	81.05	19.99	0.12	96.8	4.5	0.0204	0.0043
*2	1	0.03497	0.02248	0.00326	4.290	113.4	20.013	0.092	90.9	5.9	0.0099	0.0012
*3	1	0.04713	0.08456	bdl	5.061	135.3	19.978	0.099	89.7	6.9	0.0315	0.0022
*4	1	0.10761	0.01469	0.00261	2.209	84.89	20.03	0.26	62.5	3.0	0.0125	0.0040
*5	1	0.47887	0.01817	0.00262	3.170	217.8	20.06	0.57	35.0	4.3	0.0108	0.0027
*6	1	0.01003	0.07354	0.00086	3.036	76.26	20.12	0.12	96.1	4.2	0.0457	0.0038
*7	1	0.00489	0.04719	0.00074	3.065	75.19	20.05	0.10	98.0	4.2	0.0290	0.0025
*8	1	0.01018	0.14663	bdl	8.070	196.8	20.008	0.077	98.4	11.1	0.0343	0.0024
*9	1	0.02552	0.07371	0.00239	5.054	127.4	19.758	0.093	94.0	6.9	0.0275	0.0023
*10	1	0.02030	0.03709	0.00027	7.233	179.7	20.013	0.091	96.6	9.9	0.0097	0.0016
*11	1	0.00581	0.01489	bdl	2.780	68.47	20.01	0.13	97.5	3.8	0.0101	0.0030
*12	1	0.02047	0.13845	0.00100	5.251	132.4	20.049	0.087	95.4	7.2	0.0497	0.0042
*13	1	0.07014	0.25224	0.00367	5.403	150.1	19.955	0.099	86.2	7.4	0.0881	0.0070
*14	1	0.01867	0.00398	0.00063	3.840	98.34	20.14	0.10	94.4	5.3	0.0020	0.0049
*15	1	0.00191	0.01517	0.00026	1.603	39.07	20.01	0.19	98.5	2.2	0.018	0.011
*16	1	0.00350	0.00540	bdl	2.171	52.86	19.89	0.16	98.0	3.0	0.0047	0.0077

**Table S1** Continued

No.	# grains weight (mg) laser power (W)	<sup>36</sup> Ar <sub>(atm)</sub>	<sup>37</sup> Ar <sub>(Ca)</sub>	<sup>38</sup> Ar <sub>(Cl)</sub>	<sup>39</sup> Ar <sub>(K)</sub>	<sup>40</sup> Ar <sub>(Tot)</sub>	Age (Ma)	±2σ	<sup>40</sup> Ar* %	<sup>39</sup> Ar <sub>K</sub> %	Ca/K	±2σ
*17	6	0.01137	0.05664	bdl	5.413	132.9	19.938	0.083	97.4	7.4	0.0197	0.0039
*18	1	0.00286	0.00750	0.00046	1.956	47.88	20.04	0.12	98.2	2.7	0.007	0.016
Total gas age							20.00	0.13				
Error-weighted mean age (17 out of 18 runs), MSWD=1.13							20.01	0.12				
isochron age ( <sup>36</sup> Ar/ <sup>40</sup> Ar vs. <sup>39</sup> Ar/ <sup>40</sup> Ar diagram), MSWD=1.20							20.01	0.13				
<sup>40</sup> Ar/ <sup>36</sup> Ar intercept							295.4	4.0				

Errors on the single runs are analytical uncertainties. Errors on total gas and error-weighted mean ages also include the uncertainty in *J* value. \*, runs used in the weighted mean calculation. bdl, below detection limit